

1 **Controls on cave drip water temperature and implications for speleothem-based**
2 **paleoclimate reconstructions**

3

4 Gabriel C. Rau^{*,1,2}, Mark O. Cuthbert^{2,3}, Martin S. Andersen^{1,2}, Andy Baker², Helen
5 Rutledge^{2,4}, Monika Markowska^{2,5}, Hamid Roshan^{1,2}, Christopher E. Marjo⁴, Peter W.
6 Graham^{2,6}, R. Ian Acworth^{1,2}

7

- 8 1. Connected Waters Initiative Research Centre, UNSW Australia, 110 King Street, Manly
9 Vale, 2093, Australia
- 10 2. Connected Waters Initiative Research Centre, UNSW Australia, Sydney, NSW 2052,
11 Australia
- 12 3. School of Geography, Earth and Environmental Sciences, University of Birmingham,
13 Edgbaston, Birmingham, B15 2TT, UK
- 14 4. Mark Wainwright Analytical Centre, UNSW Australia, Sydney, NSW 2052, Australia
- 15 5. Australian Nuclear Science and Technology Organisation, Lucas Heights NSW 2234,
16 Australia
- 17 6. SGA Environmental, Suite 8, 599 Pacific Highway, St Leonards, NSW 2065, Australia

18

19 * Corresponding author:

20 Gabriel C. Rau (gabriel.rau@unsw.edu.au)

21 UNSW Australia, 110 King Street, Manly Vale NSW 2093

22 Phone: +61 2 80719850, Fax: +61 2 9949 4188

23

24 **KEYWORDS:** Drip water temperature, speleology heat transport, paleoclimate archive,
25 speleometeorology.

26

27 Invited to the thematic speleothem issue, "Novel approaches to and new insights from
28 speleothem-based climate reconstructions", in *Quaternary Science Reviews*. Guest editors:
29 Corinne I. Wong and Daniel O. Breecker (QSR Editor Claude Hillaire-Marcel)

30 **Abstract**

31 While several studies explore cave climate and thermal regimes, little is known about the
32 controls on cave drip water temperature. Yet water temperature significantly influences
33 biogeochemical processes associated with cave drips. To identify the processes that control
34 the cave drip water temperature, we measured the temperatures at multiple locations along a
35 speleothem flow path and drip sources (stalactites) concurrently with the drip rates in
36 Cathedral Cave, Wellington, Australia. We monitored long-term drip water temperature, drip
37 rates, surface and cave climate and in-cave evaporation rates and conducted 3 infiltration
38 experiments with different flow, temperature and isotopic conditions. Our results show that
39 the drip water temperature is controlled by multiple superimposed heat transport mechanisms
40 that act upon the infiltrating water in the epikarst, the water film after it enters the cave and
41 before it becomes a drip. The two main heat sources/sinks for drip water are the cave air and
42 the surrounding rock. The subsurface temperature is coupled to the surface temperature by
43 conduction through the soil and rock mass, but the cave climate is also coupled to the surface
44 climate by venting. On a regional scale drip temperatures are mainly driven by the annual
45 ground surface temperature signal but damped with depth and shifted in time compared to the
46 surface. On a local scale, the drip water temperature can differ significantly from cave air and
47 speleothem temperature due to the latent heat exchange of evaporation and localised water
48 film convection. The main controls are ground surface temperature, subsurface depth, air
49 density induced ventilation, distance from entry and drip rate. We present a conceptual model
50 that explains drip water temperature signals and provide signal driven guidance on best type
51 and location for speleothem sampling. We anticipate that our results will significantly
52 improve the understanding of temperature-dependent paleoclimate signals from speleothem
53 archives.

54 **1. Introduction**

55 **1.1. Context and Aims**

56 Surprisingly little work has been done on what controls the temperature of cave drip water
57 and yet this is of fundamental importance as it controls biogeochemical processes in caves.
58 For example, drip water temperature influences the growth rate of speleothems [Dreybrodt,
59 1981; Baker et al., 1998], fractionation of isotopes [Epstein et al., 1953], and deposition of
60 biomarkers [Schouten et al., 2007]. In speleometeorology, latent heat exchange processes
61 such as condensation or evaporation alter the thermal energy content of drip water [De Freitas
62 and Schmekal, 2003] and can lead to cooling of speleothems [Cuthbert et al., 2014a]. Finally,
63 in geomicrobiology, the habitat of cave microorganisms is strongly influenced by temperature
64 [Northup and Lavoie, 2010].

65 Cave drip water originates from precipitation or surface flow, which infiltrates the soil
66 surface. It is well recognised that the dynamic temperatures at the earth's surface propagate
67 into the subsurface [Stallman, 1965; Baker and Ruschy, 1993]. Near-surface temperature
68 measurements can be used to quantify water flow [Rau et al., 2014], for example by
69 exploiting temperature-time variations [Taniguchi and Sharma, 1993; Bendjoudi et al., 2005]
70 or temperature depth profiles [Tabbagh et al., 1999; Cheviron et al., 2005]. Fluctuating
71 ground surface temperatures are damped with depth until a stable temperature is reached
72 [Taniguchi, 1993; Smerdon et al., 2003]. The dominant mechanism of subsurface heat
73 transfer beyond the soil zone is by conduction [Smerdon et al., 2003]. However, the influence
74 of rock, as opposed to air, temperature profiles on cave drip water temperature has not been
75 investigated.

76 Water commonly flows over speleothem surfaces such as flowstones, stalactites and draperies
77 inside caves before arriving at the drip source (falling films) [i.e., Camporeale and Ridolfi,
78 2012]. During film flow a number of different heat and mass transfer mechanisms act
79 simultaneously. While the engineering literature reports on simultaneous heat and mass
80 transfer during film flow [i.e., Yan and Soong, 1995], cave related sciences have not
81 investigated the effects of film flow heat transport on the cave drip water temperature. Yet it
82 is well accepted that water films will exchange moisture and heat with the cave air [Atkinson
83 et al., 1983; Faimon et al., 2012].

84 Cave water is generally in contact with cave air for some time before forming drips. Cave
85 climate must therefore be considered when investigating what controls cave drip water
86 temperatures for caves that are open to the atmosphere. It has been shown that surface air

87 temperature anomalies can affect cave air temperature [Dominguez-Villar et al., 2013, 2014].
88 A change in cave climate is associated with advective air flow by venting [De Freitas et al.,
89 1982; De Freitas and Littlejohn, 1987]. Cave venting is caused by barometric pressure
90 changes, density differences between cave and surface air (chimney effect) [Conn, 1966;
91 Wigley, 1967; Oh and Kim, 2011] or through winds across the entrances (venturi effect)
92 [Kowalczk and Froelich, 2010]. Cave-atmosphere air exchange results in spatiotemporal
93 variability of otherwise stable cave air temperature [Smithson, 1991; Perrier et al., 2010]. In a
94 comprehensive investigation of cave air venting Faimon et al. [2012] determined the key
95 drivers of the microclimatic variability.

96 The cave climate also responds rapidly but predictably to changing atmospheric climate
97 conditions [Atkinson et al., 1983; De Freitas and Littlejohn, 1987]. Air flow can cause
98 significant loss of water due to evaporation from caves [McLean, 1971] with increasing
99 moisture loss for only small decreases in cave relative humidity below the saturation point
100 [Buecher, 1999]. Cuthbert et al. [2014a] reported significant cooling of speleothems, and drip
101 water, through in-cave evaporation.

102 Conversely, cave condensation and its change to the overall thermal energy balance were also
103 found to relate to cave air temperatures [De Freitas and Schmekal, 2003]. Condensation can
104 increase the temperature of cave walls [Dreybrodt et al., 2005]. Further, considerable
105 speleothem dissolution can be caused by condensation through the formation of calcite
106 undersaturated drips [Rozemarijn et al., 1998]. Importantly, cave climate exerts significant
107 control on speleothem deposition through the temperature dependence of both kinetic and
108 equilibrium drip water geochemical processes [Spötl et al., 2005; Baldini et al., 2008].
109 However, the in-cave climatic controls on cave drip water temperature have also yet to be
110 explored systematically.

111 When considering temperature as a control for water related cave processes and the
112 interpretation of temperature-dependent speleothem paleoclimate proxies, the cave air
113 temperature is generally used, since it is easily measured. Here, we illustrate that the true
114 cave drip water temperature can differ significantly from cave air temperature and we
115 identify the processes exerting control. Hence the aim of this paper is to identify and describe
116 the controls on cave drip water temperature. We systematically investigate the dominant
117 influences on cave thermal regimes and drip water temperature by analysing subsurface heat
118 (and mass) transport through the karst and the atmospheric connection. Examples for the
119 different controls are presented using measurements of drip rate, speleothem and drip water

120 temperature as well as climate data monitored inside the cave and on the land surface. Using
121 this data we demonstrate how a surface air temperature climate signal will be propagated to a
122 cave, and how the resulting drip water temperatures may deviate from the mean annual air
123 temperature.

124 **1.2. Description of the field site and prior work**

125 Data presented in this paper was acquired at Cathedral Cave in the Wellington Caves Reserve
126 (Latitude -32.622°, Longitude 148.940°) in New South Wales, Australia. Figure 1 shows the
127 location and horizontal dimensions of Cathedral Cave. Cathedral Cave is located in a
128 temperate semi-arid zone. The Caves Reserve is exposed to a significant seasonal variation in
129 the surface air temperature between approx. 0 to 45 °C, with a mean annual maximum
130 temperature of 24.3 °C. Long-term annual average rainfall in the area is episodic with approx.
131 617 mm/year, and the relative humidity varies between 6-98 % with a mean annual value of
132 68 % [BOM, 2014].

133 The cave system is located in the Molong Anticlinorial Zone and intersects a massive and
134 thinly bedded Devonian limestone [Osborne, 2007]. Cathedral Cave is one of the larger caves
135 featuring two nearby entrances and has a vertical depth of approx. 25 m. As a show cave it is
136 well-developed with infrastructure suitable for tourist groups. The cave is easily accessible
137 and offers an ideal opportunity to investigate subsurface karst processes, such as karst
138 hydrology, geochemistry and paleoclimate signals in speleothems. The cave has been subject
139 to long-term drip rate and drip water monitoring starting in 2009 and ongoing. Jex et al.
140 [2012] correlated spatially distributed drip records and found that they group into distinct
141 categories of differently behaving clusters indicative of the flow path features. Mariethoz et
142 al. [2012] identified chaos in drip rates and concluded that this contains information about
143 flow routing in fractured media. Rutledge et al. [2014] found clear soil and limestone
144 signatures in the drip water through trace elements and organic matter analysis. Cuthbert et
145 al. [2014b] reported that cave drip water is only activated after long duration and high volume
146 rainfall, and that evaporation from the epikarst is an important control on drip water isotopic
147 composition.

148 **2. Materials and methods**

149 **2.1. Surface irrigation**

150 Owing to the temperate semi-arid climate at the Wellington Caves Reserve, rainfall events
151 sufficient to overcome the soil moisture deficit and trigger cave dripping are erratic [Jex et
152 al., 2012; Mariethoz et al., 2012]. To induce dripping in the shallow cave so that controls on
153 cave drip water temperature could be investigated a total of 3 controlled surface irrigation
154 experiments were conducted over a two-year period (2013-2014). Geochemical results of the
155 first irrigation experiment were previously published in Rutledge et al. [2014] and drip water
156 temperature data from the second irrigation experiment has been reported in Cuthbert et al.
157 [2014a].

158 During the surface irrigations a patch size of $\sim 24 \text{ m}^2$ (2013) and $\sim 50 \text{ m}^2$ (2014) above the
159 near-surface chamber of Cathedral Cave (see Figure 1) was hand hosed with town water from
160 a storage tank. Two summer and one winter irrigation campaigns were conducted. The dates
161 and specifics of each of the three surface irrigation experiments are summarised in Table 1.
162 Importantly, during the first irrigation experiment, the temperature of first and third
163 continuous surface application was set to approx. $0.3 \text{ }^\circ\text{C}$ using ice bags. Further, deuterium
164 was added as a conservative tracer to the batch of water first applied (enrichment of $\sim 6100 \text{ } \%$
165 VSMOW) during surface irrigation in 2013. Markowska et al. [submitted] provide a detailed
166 analysis of the deuterium tracer measured during the same experiments as well as long-term
167 monitoring of natural isotopic composition.

168 **2.2. Cave and surface monitoring**

169 Different sites were selected for monitoring at increasing cave depths and distance from cave
170 entrance (Figure 1). To measure the drip water temperature we affixed automated miniature
171 temperature loggers (DST micro T, StarOddi, Iceland) along known flow paths of water on
172 top of the speleothem (flowstone), with a logger mounted to the tip of the drip source
173 (stalactite, Figure 2B). The loggers were selected based on their small size, rapid temperature
174 response time ($\sim 20 \text{ s}$), resolution ($0.01 \text{ }^\circ\text{C}$) and accuracy ($\pm 0.2 \text{ }^\circ\text{C}$). These features make the
175 loggers an ideal choice for monitoring drip water temperature. The cave air temperature was
176 also measured in close proximity to the drip source (Figure 2A). During the irrigation
177 experiment in January 2013 (southern hemisphere summer) the shallow soil temperature of
178 the irrigation patch was monitored at 2 locations with DST micro T loggers (Figure 1).

179 In the January 2014 irrigations, in addition to the StarOddi loggers, detailed temperature
180 measurements were acquired with high accuracy ($\pm 0.002 \text{ }^\circ\text{C}$) and resolution ($0.0006 \text{ }^\circ\text{C}$)

181 custom-build instrumentation. The sensors consisted of Platinum resistors (Pt1000, 1 k Ω at 0
182 $^{\circ}$ C) embedded in flat aluminium housing (25 x 6 x 1 mm – see Figure 2C) designed for fast
183 thermal response. Figure 2 shows sensors deployed along a flow stone and stalactite near the
184 entry (site A, location in Figure 1). More details about method and results from this
185 deployment are reported in Cuthbert et al. [2014a]. Here, we use a subset of this data for a
186 more detailed and comprehensive description of the heat transport processes that exert control
187 on cave drip water temperatures.

188 The drip locations were also monitored continuously with automated drip counters
189 (Stalagmate, Driptych, UK). Further, climate monitoring stations consisting of relative
190 humidity and temperature sensors (HMP155A, Campbell Scientific, USA) were deployed at
191 2 different locations to record the cave air. Cave barometric pressure was also measured
192 using a pressure transducer (Levellogger, Solinst Inc., Canada). Water samples were
193 regularly collected from drip sources at site A with 20 ml glass McCartney bottles. The
194 samples were analysed using a Los Gatos $^{\circ}$ cavity ring down laser spectrometer with overall
195 precision of $\pm 2.0\%$ $\delta^2\text{H}$. Evaporation pans (9.5 cm inner diameter) were deployed at site A
196 and C (Figure 1) for extended periods of time. Volumetric water loss was measured using a
197 digital pipette, precision scale and the pan size, and the evaporation rate was calculated from
198 the time of pan deployment.

199 Surface climate variables, i.e. air temperature, shallow soil temperature and moisture, relative
200 humidity and barometric pressure, were monitored by a climate station (Hill Climate Station,
201 Wellington, data download available: <http://groundwater.anu.edu.au/>) located in close
202 proximity south-east of Cathedral Cave. Precipitation data was recorded by a rain gauge in
203 Wellington ~6.5 km away (Agrowplow, station 065034) [BOM, 2014]. The thickness of the
204 soil zone was found to vary from 0 to 0.5 m estimated by inserting a thin metal rod into the
205 soil across the irrigation patch. During the 2014 experiment volumetric soil moisture
206 integrated across the upper 10 cm was measured frequently at random spots across the
207 irrigation patch with a handheld meter (MPM160, ICT International, Australia).

208 **2.3. Data processing**

209 **2.3.1. Surface to subsurface heat conduction**

210 The Earth's surface is exposed to time variable heat influx from solar radiation, which forms
211 a significant energy source for subsurface propagation. The periodicity of insolation is
212 controlled through the earth and solar cycles. Hence, surface air temperature contains distinct
213 frequencies, i.e. daily, annual, decadal, centennial, millennial, as well as aperiodic

214 environmental influences related to local weather and climate, i.e. high and low pressure
 215 systems, and oscillation indices. Cave temperatures have been related to ground surface and
 216 surface air temperatures by analysing heat propagation with depth through conduction
 217 assuming that thermal properties can be depth averaged [Smerdon et al., 2003, 2004].

218 Carslaw and Jaeger [1959] formulated a 1D differential heat conduction equation. The
 219 equation was solved with a harmonic temperature boundary at the top and a constant
 220 temperature boundary at infinite depth. This resembles the subsurface environment between
 221 surface and cave. Since the heat transport equation is of linear nature, the analytical solution
 222 is valid for any harmonic component of temperature variation with an individual frequency
 223 (e.g. daily or annual) that is part of the total temperature signal [Goto et al., 2005].

224 Here, we consider that thermal diffusivity for soil can vary due to differences in saturation
 225 [Ochsner et al., 2001], compared to low porosity bedrock which can be assumed to be
 226 constant over time. Consequently, it is useful to separate the subsurface into two layers: soil
 227 zone and epikarst zone. While several studies have used shallow multi-level soil temperature
 228 measurements to calculate near-surface infiltration [Smerdon et al., 2004; Bendjouidi et al.,
 229 2005; Cheviron et al., 2005] the propagation of thermal waves into rock above the
 230 groundwater table is predominantly controlled by thermal diffusion [Smerdon et al., 2003].

231 To calculate the dynamic subsurface rock temperature through two layers, an analytical
 232 solution [Carslaw and Jaeger, 1959; Goto et al., 2005] is modified as

$$233 \quad (1) \quad T_i(z, t) = T_0 + A_i \cdot \exp\left(-\sqrt{\frac{\pi}{P_i}} \left(\frac{d_s}{\sqrt{D_s}} + \frac{z-d_s}{\sqrt{D_r}}\right)\right) \cdot \cos\left(2\pi \frac{t}{P_i} - \sqrt{\frac{\pi}{P_i}} \left(\frac{d_s}{\sqrt{D_s}} + \frac{z-d_s}{\sqrt{D_r}}\right) - \theta_i\right)$$

234 for $z \geq d_s$. Here, i is a distinct harmonic temperature component with period P_i [d]. T_i is the
 235 temperature [°C] due to harmonic temperature component i as a function of depth z below
 236 subsurface [m] and t is time [d]; T_0 is the mean surface temperature [°C]; A_i is the amplitude
 237 [°C] of the harmonic signal i ; θ_i is a phase offset [rad]; d_s is the thickness of the soil layer
 238 [m].

239 In Equation 1, D is the effective thermal diffusivity for the soil layer (subscript s) and the
 240 epikarst (subscript r). In general, the thermal diffusivity [m²/d] is defined as [Carslaw and
 241 Jaeger, 1959]

242 (2)
$$D = \frac{\kappa}{\rho c}$$

243 where κ is the bulk thermal conductivity [W/m/K] for variably saturated soil or solid rock [de
244 Vries, 1963; Tarnawski, 2011; Horai, 1971; Clauser and Huenges, 1995]. Analogously, the
245 bulk volumetric heat capacity ρc [MJ/m³/K] is reported for sediments and rock [Schön, 1996;
246 Schärli and Rybach, 2001].

247 Equation 1 can be used to predict the subsurface temperature response to a particular
248 frequency component of interest extracted from the ground surface temperature data. For
249 example the i -th component could be daily, annual, centennial, millennial, or any other
250 significant component determined using a Fourier transform analysis of dominant
251 frequencies. In Equation 1 the exponential part accounts for temperature amplitude damping
252 and the cosine part for the shift in phase over depth. The phase offset θ is the time relative to
253 the maximum insolation (summer solstice on 21 December in the southern hemisphere) and
254 accounts for any difference between the conduction theory and realistic conditions.

255 In this paper we use 2 different layers, one representing the soil and one the limestone. We
256 measured the thermal conductivity and heat capacity of soil and limestone samples collected
257 at the Cathedral Cave field site (Figure 1) using a KD2 Pro thermal analyser (Decagon
258 Devices, US). To account for the variable water saturation of the soil (i.e. dry and saturated
259 end members), the soil parameters were measured after oven drying (105 °C, 6 hours) and
260 after saturating the soil sample with water. Further, a piece of limestone bedrock had holes
261 drilled for inserting the instrument needles, and a highly conductive paste was used to ensure
262 optimal thermal bridging between needle and limestone sample. The measured thermal
263 parameters are listed in Table 2.

264 Equations 1 & 2 were used to simulate the annual temperature variations (with $P = 365.25$ d)
265 at various depths of interest. Models were fitted to temperature observations by varying
266 parameters as outlined in Table 4 and minimising the normalised root mean square error
267 (NRMSE). For the surface air temperature the parameters of interest were mean annual
268 temperature (T_0), amplitude (A) and phase offset from solstice (θ) while the depth was set
269 to zero ($z = 0$). For the cave air and flowstone temperatures the parameters of interest were
270 mean annual temperature (T_0), depth of limestone (z) and phase offset (θ). Here, the
271 remaining parameters were set as follows: Amplitude A as determined from the surface air

272 temperature fit, soil zone thickness $d = 0.1$ m, thermal diffusivities as measured on soil and a
273 limestone sample (Table 2).

274 **2.3.2. Air density calculation**

275 A well-known process of cave atmosphere air and moisture exchange is venting stimulated
276 by the difference in density between atmospheric and cave air (the chimney effect) [Conn,
277 1966; Wigley, 1967; Oh and Kim, 2011]. The density of air can be calculated taking into
278 account thermodynamic properties of dry air as well as water vapour [Giacomo, 1982]. It is
279 expressed as

$$280 \quad (3) \quad \rho_a = \frac{pM_a}{ZRT} \left[1 - x_v \left(1 - \frac{M_v}{M_a} \right) \right]$$

281 where p is the barometric pressure [Pa]; Z is the compressibility coefficient, under the
282 conditions reported here of value 0.999611566 [-]; R is the universal gas constant, 8.31441
283 [J/K/mol] and T is the temperature [K]; M_a and M_v are the molar mass of dry air
284 0.0289635 [kg/mol] and water vapour 0.018015 [kg/mol]. The mole fraction of water vapour
285 in moist air x_v is defined as

$$286 \quad (4) \quad x_v = \frac{h}{p} \exp(AT^2 + BT + C + DT^{-1})f$$

287 where h is the relative humidity ($0 < h < 1$); f is an enhancement factor, under the
288 conditions reported here of value 1.0038 [-]; the saturation vapour pressure coefficients are
289 published as $A = 1.2811805 \cdot 10^{-5}$ [K⁻²], $B = -1.9509874 \cdot 10^{-2}$ [K⁻¹], $C = 34.04926034$,
290 $D = -6.3536311 \cdot 10^3$ [K]. For above parameter values please refer to Giacomo [1982].

291 Equations 3 and 4 require measurement of the common variables that define the
292 thermodynamic state of moist air: barometric pressure, air temperature and relative humidity
293 (RH). To investigate cave venting, air densities were calculated from the surface and cave
294 climate records for a 2-week period during both summer and winter in 2014.

295 **3. Results**

296 **3.1. Surface and cave climate**

297 Figure 3 shows surface air temperature and rainfall recorded at the surface above Cathedral
298 Cave over a 2-year period between 2012 and 2014. Cave air temperature measured near site
299 A is also shown. A climatic summary for the period between Jan 2013 and Dec 2014 is as
300 follows: The minimum and maximum surface air temperatures were -2.9 °C and 43.5 °C.
301 Typical for a temperate semi-arid climate, relative humidity varied between 5-98 %, with a
302 median of ~63 %. For more than half of the year (233 d) the volumetric soil moisture content
303 was below the median annual value of 21 % because evapotranspiration generally exceeds
304 precipitation.

305 While ~312 days/year were without significant rain (< 1 mm/day), below average yearly total
306 of 550 mm was recorded from episodic rainfall events occurring on 86 days/year. On 1
307 March 2013 a maximum daily rainfall of 74 mm was recorded. The amount of rain from this
308 natural event was comparable to the manual application of water on the irrigation patch
309 during the surface irrigation experiments (Table 1 and Figure 1).

310 At Site C, the air and speleothem temperature was very stable at 17.8 °C with only minor
311 fluctuations of ~0.1 °C between January-December 2014. Cave relative humidity (RH) was
312 measured at 10 min intervals during parts of the year between January and November 2014.
313 The RH, recorded at site A, fluctuated significantly with minimum, maximum and median
314 values of 59.3 %, 97.9 % and 88.6 %, respectively. At site C the RH showed very minimal
315 fluctuations around a median value of 97.1 %, with minimum and maximum RH of 96.5 %
316 and 97.8 %, respectively. Evaporation rates as measured at the different locations (Figure 1)
317 during summer and winter 2014 are shown in Table 3. There is a clearly decreasing trend in
318 evaporation rate with increasing distance from entrance in summer, with RH values
319 increasing as expected. Noteworthy, however, is the stable but below saturation RH level at
320 site C leading to some potential for evaporation from the deepest part of the cave throughout
321 the year.

322 **3.2. Drip water temperatures during irrigation experiments**

323 Figure 4 presents high resolution temperature measurements, drip counts and relative
324 humidity measured during irrigation experiment 2 conducted in January 2014 (summer).
325 While the majority of the measurements in Figure 4 were previously published by Cuthbert et
326 al. [2014a], we use this dataset as a starting point and present new results that reveal a
327 detailed analysis of the different controls on cave drip water temperature.

328 Before the first surface irrigation the soil moisture across the irrigation patch was between 4-
329 24 % indicating a high soil moisture deficit. Approx. 3 h after the start of the water
330 application (~68 mm rainfall equivalent) the drip source responded with a rapid increase to
331 approx. 140 drips/min (Figure 4B). Before the second irrigation the soil moisture was much
332 higher with measurements ranging between 20 % and 37 %. After applying less water in the
333 second irrigation (equivalent of ~48 mm rain) the drip source responded much quicker (~1 h
334 after start) and showed significantly faster drip frequency (~180 drips/min) and longer drip
335 activity compared to the previous day (Figure 4B).

336 Before the onset of dripping, temperature measurements taken on the dry speleothem surface
337 along the expected drip water flow path (Fig. 2a) were relatively constant in time but with
338 decreasing temperature from cave ceiling to drip source (stalactite) revealing a downward
339 gradient approx. $-0.8\text{ }^{\circ}\text{C/m}$ (Figure 4A). Measured air temperatures reflect a spatial gradient
340 that was similar to the one measured on the rock surface. Relative humidity measurements
341 (RH) varied between a minimum of 79 % and a maximum of 91.5 %. A spot measurement
342 near the chamber ceiling revealed RH of up to 98 % after the flowstone had been wet at the
343 end of the irrigation experiment in Jan 2014.

344 Temperatures, measured after activation of cave dripping, exhibit a rapidly increasing
345 temperature on all sensors, peaking at approx. $\sim 0.3\text{-}0.8\text{ }^{\circ}\text{C}$ above the original measurement
346 coinciding with a peak at the maximum drip count (Figure 4A). This is followed by a slow
347 temperature decrease as the drip rate decreases. At ~ 20 drips/min, the drip water
348 temperatures measured by the lower sensors returned to the level measured before the onset
349 of flow.

350 After a period of relatively stable measurements, the drip water temperature started to
351 decrease, with lower sensors showing a more rapid and pronounced cooling of up to $1.5\text{ }^{\circ}\text{C}$
352 below the cave air temperature which was measured in close proximity. The onset of

353 observable evaporative cooling was at a RH of 90 %, and the increase in drip water cooling
354 coincided with a rapid drop of RH to 79 %.

355 After the second surface irrigation the same temperature increases were observed but with
356 stronger magnitude and longer duration, despite the application of less water at the surface.
357 However, evaporative cooling was less pronounced reflecting the higher levels of RH (85-90
358 %) during this event compared to the first event.

359 Figure 5 summarises temperature and deuterium data as well as drip counts measured during
360 irrigation experiment 1 conducted in January 2013. Note that the experimental procedure and
361 measurement setup differed compared to experiment 2 described in the last section. Here,
362 drip water temperature was only measured at the drip source (same stalactite as above).
363 However, in addition shallow soil temperatures (~5 cm and ~10 cm below the surface) were
364 measured, but cave air RH was not. It is noteworthy that 4 individual irrigations were applied
365 (35-63 mm rainfall equivalent) and with the water during the first 3 applications cooled to ~0
366 °C, ~10 °C and ~0 °C, respectively.

367 Cave air temperature was relatively stable at approx. 17.5 °C (Figure 5A), while the daytime
368 outside air temperature peaked at approx. 40 °C. During the time of experimentation the cave
369 air temperature shows slight increases during the times at which the surface air temperature
370 was at its lowest (night time). This excludes one occasion on 10 January 2013 where the cave
371 air and drip water temperatures both decreased coincident with the surface air temperature
372 falling below the average cave temperature (grey arrow in Figure 5B). Also noteworthy here
373 is the response of the soil temperatures to the cooled irrigation water, with both sensors
374 showing measurements as low as 5 °C and 14 °C which are clearly below the minimum
375 surface air temperature of 15 °C during that time (Figure 5A).

376 Drip water temperatures responded similarly to the surface irrigation during the January 2013
377 experiment (Figure 5D) compared to the experiment in 2014 (Figure 4B). Interestingly, the
378 drip water temperature at the first drip activation with an average drip response of 80
379 drips/min shows a cooling event during which there was a significant temperature difference
380 of -2.5 °C between drip water and air temperature (Figure 5B). This was the response to an
381 irrigation application where the water was cooled to 10 °C, less than during the first irrigation
382 (Figure 5A). A similar sized evaporative cooling event can be seen again during the drip
383 recession caused by the last surface irrigation where ~24 °C water was applied without the
384 addition of ice. A clear deuterium enrichment (deuterium breakthrough) was measured in drip

385 water samples after the third surface application originating from the deuterium that was
386 added to the first irrigation batch (Figure 5C).

387 Drip water temperature after the third surface irrigation during which water was cooled again
388 to 0 °C showed a very small decrease before warming and tracking close to the cave air
389 temperature (Figure 5B). As soon as the drip rate fell below ~30 drips/min another
390 evaporative cooling event was observed. This time, however, it was overwhelmed by the last
391 surface application of water which carried warm water as film flow along the speleothem
392 surface.

393 **3.3. Long term air, speleothem and drip water temperature records**

394 Figure 6 shows the temperature data measured on the speleothem surface (dry or wet cave
395 over speleothem surfaces) at three different locations along the drip water flow path at site A
396 (see Figure 2) including the drip source (stalactite), air temperature and drip rate over a time
397 period of ~11 months. Figure 6 includes the response to surface irrigation experiment 3 (also
398 highlighted in Figure 3). The trend in all temperature data complies with a distinct annual
399 harmonic but with different amplitude and phase compared to surface air temperature. This
400 originates from subsurface conduction of the annual surface temperature wave, and we will
401 refer to this as the “background temperature”.

402 Results from fitting surface air, cave air, speleothem and drip water temperature time-series
403 to Equation 1 with an annual periodicity are presented in Table 4 ordered by increasing total
404 depth. The best fitting annual harmonics are also plotted in Figures 3 and 6. Noteworthy here
405 is the characteristic amplitude damping and phase shifting with increasing total depth. While
406 the surface air temperature is offset from summer solstice by 20 days, there is a relatively
407 constant phase offset of ~11 to 12 days (compared to the surface air temperature) once the
408 annual temperature harmonic propagated through the subsurface. This indicates compliance
409 with the subsurface heat conduction theory (Equation 1). Further, total depths obtained from
410 the fitting procedure are in good agreement with the vertical cave dimensions estimated from
411 an in-cave survey (Figure 2A).

412 The two upper measurement points show relatively stable temperature over time, when
413 considering faster than annual frequencies, but with occasional upward and downward spikes
414 indicating fast advective film flow in summer and winter, respectively. However, the
415 temperature measured in air and the tip of the stalactite (Figure 2) shows marked fluctuations
416 with a daily frequency and varying amplitude of up to ~1 °C superimposed on irregular lower

417 frequency variations and the background temperature. A number of drip events with varying
418 magnitude and with a maximum of ~25 drips/min were recorded (Figure 6). At this point a
419 question arises: What causes the faster than annual temperature fluctuations?

420 **3.4. Examples of venting induced drip temperature changes**

421 Figure 7 shows a detailed snapshot of cave flowstone, 2 stalactites, and cave air temperature
422 (A, D) as well as cave RH (B, E), and surface and cave air density calculated using Equations
423 3-4 (C, F) during summer and winter in the year 2014.

424 In summer (Figure 7A-C), a small drip event triggered an upwards temperature spike ~0.5 °C
425 on the stalactite, followed by multiple cooling fluctuations with magnitude ~1.5 °C
426 coinciding with rapid decreases in cave air RH due to the venting events. A decrease in cave
427 air temperature, with some delay, as a result of evaporative cooling, is also evident from the
428 data. The cooling events are similar to those observable during the irrigation experiments
429 (Figures 4A and 5A) but seem to occur with a daily frequency over certain periods (Figure 6).
430 When comparing this with the surface and cave air densities it is clear that the regular RH
431 decreases correlate well with periods where the surface air is denser than the cave air (note
432 that dry air is denser than humid air of the same temperature) in the early mornings causing
433 frequent cave venting events. Interestingly, evaporative cooling spikes also occur higher up
434 the profile where the drip water flows as a film along the speleothem surface (Figure 6).

435 Figure 7D-F contains the 2 weeks of winter monitoring that also coincide with the third
436 surface irrigation experiment 3. In winter (Figure 7D-F) the drip source shows regular daily
437 temperature fluctuations of ~0.8 °C. Inspection of cave climate parameters reveals that the
438 cave air temperature fluctuates more and the RH less compared to summer (Figure 7E vs 7B).
439 Further, the outside air is almost continuously denser than the air in the shallow entrance area
440 (Figure 7F). Interestingly, the drip water temperature mainly reflected the pattern of the cave
441 air temperature while the drip rate (resulting from artificial surface irrigation during winter)
442 did not exceed ~25 drips in a 15 minute interval.

443 **4. Discussion**

444 Results presented in this paper allow, for the first time, a detailed identification of what
445 controls the temperature of cave drip water. First we identify the controls and analyse how
446 they affect drip water temperature, then we discuss their significance and implications in
447 relation to interpreting speleothem records as paleoclimate archives.

448 **4.1. What mechanisms control the cave drip water temperature?**

449 Water movement to the drip source often occurs as film flow on cave deposits along variable
450 distances [Dreybrodt et al., 2005; Camporeale and Ridolfi, 2012; Baker et al., 2014]. The data
451 presented here demonstrates that cave drip water temperature is controlled by a number of
452 simultaneous heat transport mechanisms that act upon the water film. Heat transfer between
453 rock and water in karst conduits was analysed in detail by Covington et al. [2011], Covington
454 et al. [2012] and Luhmann et al. [2015]. Dreybrodt et al. [2005] have theoretically analysed
455 the heat and mass interactions involved in condensation corrosion involving water films. The
456 engineering literature has recognised the complexity of film flow heat and mass exchange
457 [i.e., Yan and Soong, 1995]. In relation to speleology our results are first in reporting and
458 analysing heat transport processes that control cave drip water temperature.

459 The variety of different mechanisms and associated variables complicates quantification of
460 the individual processes. Here, we focus on a detailed description of temperature
461 characteristics that can be measured after water enters the cave and flows along cave features
462 before arriving at the drip source. Figure 8 conceptualises the controls on drip water
463 temperature. The individual heat transport mechanisms are discussed with reference to
464 examples presented in the results.

465 **Convective heat transport:**

466 Heat convection due to subsurface water percolation ($q_{f, surf}$):

467 During the first surface irrigation experiment the water was deliberately cooled (Table 1) to
468 test whether its thermal signature, transported by heat convection through the soil zone and
469 the epikarst stores, is detectable at the drip source. The pre-existing large soil moisture deficit
470 prior to surface irrigations was responsible for the first irrigation not producing any flow in
471 the cave (Figure 5A). Due to the hot weather and general heat conduction towards the
472 irrigated patch the cooled soil recovered to near normal temperatures between each of the
473 cooled irrigations. While the second application was cold enough (~ 10 °C) for the thermal
474 signature to be seen in the soil zone the cooling anomaly observed at the drip source

475 (locations k1 and k2 in Figure 5B) did not originate from the cooled surface irrigation. The
476 main evidence for this conclusion is the lack of breakthrough of the deuterium enriched water
477 (~6100 ‰ VSMOW) from the first irrigation (Figure 5C). The breakthrough of deuterium
478 occurred after the third irrigation, indicating that the water travel time was significantly
479 longer than the time between individual irrigations and the corresponding drip response in the
480 cave. Markowska et al. [submitted] concluded that the water activating the drip came from
481 epikarst stores. This also means that convection of cold water from the surface to the cave
482 will take longer than the individual drip response time.

483 While the soil zone clearly responded to the three applications of cooled water at 2 separate
484 locations (Figure 5A), the only signature attributable to the ice water detected at the drip
485 source was a sharp short temperature fluctuation of only -0.8 °C on 10 Jan 2012 at 09:18
486 while the air temperature remained constant (blue arrow in Figure 5A). Importantly, this
487 happened at a time during which fast film flow occurred over the flowstone, so this is not a
488 temperature signal attributable to evaporative cooling (which only is dominant at slower
489 flow). Interestingly, this short lasting cooling event was detected shortly after the start of the
490 third surface irrigation (~35 mm rainfall equivalent) with ice-cooled water (~0 °C) while the
491 soil was still cooled from the previous event. We interpret this as heat convection due to
492 subsurface water percolation caused by fast preferential flow through the well wetted soil and
493 fracture flow in the epikarst below. Note that first breakthrough of deuteriated water from the
494 first surface irrigation was observed at the same time (Figure 5C and Markowska et al.
495 [submitted]).

496 The above discussion illustrates that drip water temperature can be affected by thermal
497 energy transported from the surface to the drip source through convection caused by
498 subsurface water percolation. However, the prerequisites are that soil moisture is at field
499 capacity, that preferential flow paths are still present and that the volume of water applied to
500 the surface is much larger than the likely event based rainfall (105 mm was the maximum
501 event based total between Oct 2011 and Dec 2014). In our case it took more than 133 mm
502 rainfall equivalent (3 irrigations) of cooled water to produce a brief and small temperature
503 anomaly. Furthermore, the experimental conditions were a worst case scenario in two other
504 ways: 1) the temperature difference between the cooled irrigation water and the soil of 20-25
505 °C was unrealistically large for natural conditions, and 2) the section of the Cathedral Cave
506 used in these experiments is very shallow with only about 1.7 m of soil and rock mass
507 between the cave ceiling and the surface.

508 We expect that heat convection from subsurface water percolation caused by preferential
509 flow through the soil and fracture flow through the epikarst can rarely cause drip water
510 temperature anomalies that are significant for paleoclimate reconstructions from speleothems
511 under realistic conditions. However, we acknowledge that this will depend on the thickness
512 of the soil and epikarst as well as the fracture network above the cave. More research is
513 needed to determine the conditions for which heat convection due to preferential or fracture
514 flow from the surface can cause temperature anomalies that are of significance for
515 speleothem-based paleoclimate reconstructions at drip sources.

516 Heat convection (q_f) due to film advection (v_f) along cave walls:

517 The mechanism of convective heat transport due to film advection is clearly illustrated in the
518 drip water temperature response during surface irrigations 1 and 2 (see labelled areas in
519 Figures 4A and 5B). Since it is summer, warmer water flows in films along the speleothem
520 surfaces (v_f) where the thermal signature from above is carried with the water film (q_f)
521 (Figures 4A and 5A). As a result of convective heat transport due to film advection the drip
522 water temperature was raised by ~ 1 °C, but only at the start of the irrigation response (fastest
523 drip rates on an event basis, here > 50 drips/min) and when a negative temperature-depth
524 gradient existed (i.e., summer).

525 Temperature sensors located in the upper part of the profile (location b and c in Figure 2A)
526 near the point at which water enters the cave detected a warmer water film compared to the
527 surrounding air (Figure 4A). This thermal disequilibrium indicates heat convection due to fast
528 preferential or fracture flow triggered by the surface irrigation [Cuthbert et al., 2014a].
529 However, it is important to note that the thermal energy causing the warming anomalies does
530 not originate directly from the water applied to the surface. Instead, the anomalies originate
531 from conduction between water film and rock higher up along the profile (explanation further
532 below). Convective breakthrough between surface and cave only occurred under extreme
533 circumstances, as pointed out in the previous subsection. The warming anomalies express a
534 temporary downward shift of the localised conductive depth profile, i.e. they represent the
535 temperature of the re-equilibration between the water film and the rock mass a short distance
536 above the point of measurement. Here, we hypothesize that the magnitude of the convective
537 signature is a function of the film advection rate (v_f proportional to the drip rate), the film
538 thickness (b) and the flow distance (L). Baker et al. [2014] measured the thickness of water
539 films on speleothems and found a dependency on the curvature and roughness of its surface.

540 Considering the number of unknowns and the fact that convective and conductive heat
541 transport are both contributing during film flow, it is highly challenging to predict the water
542 temperature as a function of distance.

543 As can be seen in the long-term drip water temperature record (Figure 6), film heat
544 convection is initiated at the onset of drip events. However, it is most pronounced at the times
545 with a large (exponential) temperature-depth gradient along the profile. This thermal gradient
546 is caused by the conduction of the annual temperature signal into the subsurface rock mass.
547 Consequently, the thermal effect of convection on drip water is a pronounced heating after
548 summer and cooling after winter solstice. Further, it is most muted around the equinoxes due
549 to a reversing temperature depth profile. Importantly, any convective influence on drip water
550 temperature caused by film advection along cave walls will be muted at depths beyond the
551 reach of the annual harmonic signal (see discussion further below).

552 Exchange of moisture (m_{atm}) and thermal energy ($q_{f,atm}$) between surface and cave:

553 When caves are open to the atmosphere air is exchanged [Conn, 1966], with the “chimney
554 effect” (caused by an unstable density difference) being a common cause of venting [i.e., De
555 Freitas et al., 1982; Oh and Kim, 2011]. Here we observe that the surface air is frequently
556 denser than the shallow cave air during summer (Figure 7C) and continuously during winter
557 (Figure 7F) which causes Cathedral Cave to be a well vented cave. At this point the question
558 arises: How deep do venting events propagate into the cave?

559 Cuthbert et al. [2014] have shown that the drip water temperatures at a continuous slow drip
560 source located ~40 m into the cave (site B) was continuously ~0.6 °C cooler than the
561 surrounding speleothem and air temperature, at a depth where conduction of heat from the
562 surface is muted and where RH values are stable at ~92 %. Further, evaporation rates
563 measured at different locations increasingly deeper in the cave show that the venting effect
564 must dampen with distance from entry, which is consistent with observations in other caves
565 [Perrier et al., 2010; Faimon et al., 2012]. However, despite the fact that the high frequency
566 venting events do not directly show up at site C (Figure 1) a potential for evaporation does
567 exist since the RH is ~97 %. Maintaining RH at less than saturation would not be possible
568 without air exchange and, thus, drier and denser surface air must continuously replace moist
569 and lighter air from deep within the cave.

570 Our findings are consistent with those from Buecher [1999] who reported a significant
571 moisture loss at an average cave RH of 99.4 % due to venting in Kartchner Caverns located

572 in semi-arid Arizona. While cave venting has previously been investigated [Smithson, 1991;
573 Tarhule-Lips and Ford, 1998; Spotl et al., 2005] and its effects on the moisture loss have been
574 analysed [McLean, 1971; Buecher, 1999; De Freitas and Schmekal, 2003], we emphasize that
575 potentially significant amounts of thermal energy in the form of latent heat continuously
576 leaves the cave in the form of water vapour. This raises the question whether ongoing
577 evaporation and associated cooling can significantly lower the overall temperatures of caves
578 as well as individual drips? This could be answered by quantifying the energy lost through
579 latent heat as a fraction of the total cave energy balance.

580 **Conductive heat transport:**

581 Conduction of the surface temperature signal into the subsurface ($q_{c,atm}$):

582 Conduction of surface air temperature signals into the subsurface is a well-accepted
583 phenomenon [Smerdon et al., 2003, 2004]. Table 4 shows that the depth propagation of the
584 annual harmonic through rock mass complies well with the theory (Equation 1). Dominguez-
585 Villar et al. [2013] made use of cave thermal anomalies, measured in the cave air, to infer that
586 vegetation change at the surface influenced subsurface conduction. Further, the signature of
587 global warming was found in cave air temperature data at a depth of 37 m [Dominguez-Villar
588 et al., 2014]. We present 2 years of surface air temperature and cave air measurements, as
589 well as 1 year of speleothem, water film and drip water temperatures at different depths along
590 a flow profile. We illustrate that Equation 1 is able to predict the subsurface penetration of
591 the annual harmonic component by conduction from the ground surface temperature signal
592 considering multiple layers with different thermal properties. This should equally apply to
593 any other harmonic contained in the surface temperature signal as long as it is of sufficient
594 magnitude and duration not to be damped beyond detectability.

595 The data shown in Figures 3 and 6 demonstrate that the penetration of the annual temperature
596 variation controls the drip water temperature at site A. The surface temperature signal
597 generates the “background” temperature for drip water, but with exponentially damped
598 amplitude and linearly shifted phase proportional with depth. Here, the differences in mean
599 annual temperature can be explained with temperature changes that are slower than annual.

600 Conduction between speleothem and water film ($q_{c,rock}$):

601 The mechanism of heat conduction between speleothem and the water film, albeit “smeared”
602 by convection, is evident from the drip water temperatures measured during both irrigation

603 experiments (Figure 4A and Figure 5A). The first irrigation experiment (cooled water was
604 applied to the surface on three consecutive days, Figure 5) clearly illustrated that the pre-
605 existing temperature-depth gradient (the subsurface temperature decreases exponentially with
606 depth in summer) warmed the infiltrating colder irrigation water by conduction to produce
607 the arrival of warm pulses on the speleothem at the onset of dripping (Figure 5B). The time it
608 took for the deuteriated water to arrive at the drip source (Figure 5C) indicates a relatively
609 long residence time of water in the epikarst stores (~48 hours), for relatively large volumes of
610 water applied and an extreme temperature difference between water and rock. This
611 demonstrates that any temperature disequilibrium between rock and water from location b
612 onwards (Figure 2) must have originated from the subsurface rock mass. During irrigation
613 experiment 2 similar increases in the water temperature were observed after dripping had
614 started. Therefore, the increase in drip temperature after flow started was caused by
615 conduction from the warmer speleothem to the water further upstream of the profile
616 (exponentially decreasing rock temperature with depth in summer), followed by convective
617 heat transfer due to film advection, and subsequent conduction from the warmer water film
618 back into the rock further downstream [Cuthbert et al., 2014a].

619 The fact that the relative magnitude of the warming anomaly remained the same for sensors
620 located further along the profile is evidence for conduction between water film and rock
621 (Figure 4A). The amount of thermal energy conducted depends on the time that the water
622 film is in contact with a particular area of speleothem, the film thickness (b) and the
623 temperature difference. The contact time is determined by the velocity of the film flow (v_f),
624 which is proportional to the drip rate measured. There is a slow temperature tailing of the
625 water film and drip temperature (Figure 4A) in all records along the flow stone (L). This is
626 caused by conduction of thermal energy from the warmer water film back into the cooler
627 speleothem when convection becomes less significant than conduction at decreasing film
628 advection (= drip rates).

629 The temperature sensors that were inserted 4 cm into the speleothem confirm that the thermal
630 anomaly caused by the flowing water film is transferred into the speleothem. These sensors
631 show a temperature damping and lag with distance into the speleothem that is characteristic
632 of heat conduction (red lines in Figure 4A). Below a certain film advection rate (~20
633 drips/min in this case), convective warming ceases to dominate and is overwhelmed by
634 evaporative cooling (the cross-over of lines e & f in Figure 4A) illustrating that there is a
635 temporary thermal equilibrium (Figure 4A). Consequently, if the water film advection rate is

636 sufficiently slow or the film is thin enough the drip water temperature is controlled by the
637 speleothem temperature but only in the absence of impacts from cave climate (i.e.
638 evaporative cooling).

639 Conduction between air and water film or rock wall ($q_{c,air}$):

640 The cave air shows a vertical temperature gradient that is similar to the subsurface rock
641 temperature gradient under stable conditions, i.e. no flow and no venting events (Figure 4A).
642 Thermal anomalies can propagate much quicker through air than rock or water because the
643 thermal diffusivity of air is approx. 22 and 146 times larger than that of the rock and water,
644 respectively (Table 2). However, the heat capacity of air is in excess of ~4,000 and ~2,500
645 times smaller than water and rock, respectively. This means that the energy contained in
646 thermal anomalies brought into the cave by air venting is effectively damped by the rock
647 [Perrier et al., 2010]. Nevertheless, an example of heat conduction between air and drip water
648 can be seen during irrigation experiment 1: A venting event transports cooler air from the
649 atmosphere into the cave temporarily lowering the temperature of the drip source by ~1 °C
650 (grey arrow in Figure 5A). The drip had ceased to be active at the time however the
651 speleothem surface was still wet.

652 During winter the cave is continuously vented and the cave air temperature fluctuates
653 periodically with varying amplitudes that depend on the surface climate (Figure 7E). This
654 thermal signature is almost exactly replicated by the drip source temperature showing the
655 mechanism of conduction between air and speleothem or air and water film (Figure 7D). The
656 magnitude of temperature variation depends on the magnitude of airflow which is
657 proportional to the air density difference [Faimon et al., 2012].

658 **Latent heat and mass transport:**

659 Latent heat ($q_{l,air}$) and mass (m_{air}) exchange between the water film and cave air:

660 Cuthbert et al. [2014a] previously demonstrated evaporative cooling of speleothem drip
661 water, by as much as -1.5 °C compared to the cave air temperature. We have shown in new
662 data presented here that this may be as high as -2.5 °C (Figure 5). This anomaly was not
663 caused by heat convection due to subsurface water percolation transporting the cooled
664 irrigation water via preferential or fracture flow between surface and cave, as deuterium
665 breakthrough had not yet occurred (Figure 5C). The cooling occurred because the previously
666 dry flowstone surface was wetted by the drip response to surface irrigation. In fact, at one

667 location (k2 in Figure 5B) cooling of the wet flowstone to below air temperature continued
668 after film flow had ceased. As the absence of dripping (and therefore film flow) rules out the
669 possibility of convective cooling from cooled irrigation water applied to the surface, the
670 cooling anomaly must be caused by evaporation.

671 In Figure 6 we present a new longer record of temperatures measured on 3 points along the
672 speleothem surface including drip source (stalactite). It is obvious that frequent evaporative
673 cooling events (Figure 7A) are directly coupled to venting events lowering the RH during
674 summer (Figure 7C). Without venting the cave air RH would reach saturation over time and
675 diminish the potential for evaporation. While Buecher [1999] found that cave evaporation
676 rates are very sensitive to changes in RH, we observe that the vapour deficit also directly
677 influences the magnitude of evaporative drip water cooling (Figures 4 and 7A-C).

678 From results presented here it is clear that air venting causes a complex thermodynamic
679 coupling of cave and surface climate that influences the cave drip water temperature. We
680 illustrate frequent and significant evaporative cooling and associated moisture exchange
681 between drip water and cave air caused by frequent exchange of humid cave air with dry
682 surface air. Dreybrodt et al. [2005] reported that cave walls can be warmed due to the release
683 of latent heat during condensation in caves located in a humid climate. While our results
684 show that in-cave evaporation can cause cooling, we anticipate that condensation could warm
685 cave drip water. We illustrate that, when venting is present, cave drip water temperature near
686 cave entrances can contain significant diurnal fluctuations or continuous cooling relative to
687 cave air whenever RH is below a certain threshold. However, for drip water temperature to be
688 affected by the cave climate it must be exposed to the cave air for some time before arriving
689 at the drip source, e.g. as a water film flowing over speleothem surfaces such as flowstones,
690 stalactites and draperies.

691 **4.2. Implications for speleothem-based paleoclimate reconstructions**

692 **4.2.1. Relationship between temperature at the surface and drip** 693 **source**

694 Drip water temperature is a key variable to be considered when the paleoclimate records are
695 reconstructed from speleothem archives. Current methods allow for paleo-temperature
696 reconstruction (i.e. from $\delta^{18}O$) with seasonal and even monthly resolution [i.e., Treble et al.,
697 2007; Orland et al., 2009]. The spatial resolution of speleothem milling, and therefore the
698 temporal resolution of climate proxies, is likely to increase in the future with the development
699 of better technologies. While the surface temperature is typically the result of interest, many

700 geochemical proxies depend on the temperature of the water at the drip source. This
701 necessitates a better understanding of processes affecting the temperature at the surface of the
702 speleothem at the time of its formation. Past surface climate estimates can be influenced by
703 assumptions about the conditions along the flow path between surface and drip source.

704 Our results demonstrate that, in the absence of cave venting and convective thermal
705 breakthrough from the surface, the drip water temperature is primarily a function of
706 subsurface heat conduction, i.e. infiltrating surface water is quickly equilibrated to the
707 subsurface temperature-depth profile. A universally applicable model to describe the
708 relationship between surface and drip water temperature in this case is the differential
709 equation for conductive heat transport [Carslaw and Jaeger, 1959]. It is important to note that
710 thermal modelling requires subsurface thermal parameters such as presented in Table 2.
711 However, these are in general reasonably well constrained and references to suitable
712 literature can be found in Rau et al. [2014]. While significant temperature anomalies due to
713 convective heat transport from the surface that could imprint on paleoclimate proxies can be
714 ruled out in our case, we note that this could be possible under different karst settings.
715 However, we expect the likeliness of such temperature anomalies to decrease with
716 increasing subsurface depth.

717 The presence of the annual temperature signal in our data (Figure 3) facilitated the use of an
718 analytical solution that is based on a harmonic temperature input at the surface (Equation 1).
719 While this solution is useful for estimating the subsurface temperature response to cyclic
720 drivers (e.g. annual, decadal, centennial or millennial), many paleoclimate events of interest
721 are based on non-cyclic changes in the surface temperature, e.g. rapid climate change
722 [Holmes et al., 2011]. Modelling the latter would require the selection of a suitable model to
723 quantify the temperature evolution between surface and drip source. For example, the
724 analytical solution used by Domínguez-Villar et al. [2013] describes the subsurface
725 temperature as a function of depth and time based on a step change in surface temperature.
726 Drip source temperature signals can be predicted from arbitrary surface temperature-time
727 signals using a time convolution of this model. Vice versa, a deconvolution can unravel the
728 surface temperature from a speleothem-based paleoclimate proxy.

729 **4.2.2. Optimising the speleothem sampling location**

730 Our measurements show that drip water temperature is controlled by a complex thermal
731 coupling between the subsurface rock background temperature driven by the ground surface
732 temperature and the cave climate driven by ventilation. This requires careful consideration

733 when deciding speleothem sampling locations. For example, the stalactite on which the drip
734 temperature was measured (Figure 2A-B) was exposed to an annual temperature variation of
735 ~ 5.21 °C as conducted from the surface but with a delay of ~ 2.6 months (80 days) compared
736 to the surface temperature signal. This is a significant variation when the temperature
737 dependency of speleothem growth is considered [Hendy, 1971; Casteel and Banner, 2014]
738 and if seasonal surface temperature is to be reconstructed.

739 Figure 9 shows the propagation of selected frequency components with an average soil zone
740 thickness of 0.1 m and an underlying epikarst to a depth of 100 m as a generic example but
741 also resembles the Cathedral Cave setting. Calculations are based on the laboratory
742 measurements of thermal parameters. Envelopes for minimum and maximum thermal
743 diffusivity for soil and bedrock as reported in the literature (Table 2) were also determined
744 for transferability of the results, i.e. when different materials are present at different field
745 sites. Figure 9 clearly illustrates the characteristic amplitude damping and phase shifting with
746 depth, inherent to the different harmonic signals. For example, it might be useful for a
747 researcher to maximise or minimise the annual temperature signal (which may determine the
748 presence of annual geochemical laminae useful for chronology building) compared to the
749 long-term paleoclimate signal. If a speleothem location was to be selected where the
750 maximum annual temperature variation should not be larger than 1 °C (0.5 °C amplitude) the
751 surface amplitude damping factor is ~ 0.059 (0.5 °C/ 8.51 °C). In the absence of venting and
752 convective heat transport through preferential or fracture flow, the desired variation is not
753 exceeded at total depths of greater than ~ 8.6 m (red dot in Figure 9A).

754 Another important consideration, when paleoclimate is to be inferred from speleothem
755 archives, is the phase shift. Again an example close to our case: A surface temperature signal
756 with centennial period is shifted by ~ 7.82 years (94 months) at 15 m depth (red dot in Figure
757 9B). Hence, this should be taken into account either when an accurate resolution of temporal
758 (i.e. seasonal) climate patterns is desired or when climatic patterns are compared to other
759 sources of information. Table 5 exemplifies minimum and maximum expected damping
760 factors and signal shifts for distinct depths extracted from Figure 9. This lag is within
761 resolution of long-record dating [Cheng et al., 2009] and could explain previous lag times
762 between drip source related signals and surface events [Domínguez-Villar et al., 2009].

763 The above discussion illustrates that the speleothem sampling location will not only depend
764 on the type of proxy (i.e., $\delta^{18}O$, $\delta^{13}C$, Δ_{47} , trace metals, organics) but also on what archived

765 harmonic signal resolution is desired. The increasing temporal resolution for drip source
766 temperature dependent proxies makes shallow sampling attractive to maximise the high
767 frequency temperature signal (i.e., seasonal to annual). However, near-entrance locations
768 require a good quantitative understanding on the influence from cave climate, such as
769 evaporation (or condensation) discussed below. Deep samples are better for long-term surface
770 dependent proxies as higher frequency temperature harmonics are essentially damped out.
771 Equations 1 and 2, as visualised in Figure 9 and Table 5, can serve as a guide for targeted
772 speleothem sampling.

773 **4.2.3. Cave venting and evaporation**

774 As a further point of discussion we illustrate that cave venting, besides influencing pCO₂
775 [Spotl et al., 2005; Baldini et al., 2008; Kowalczyk and Froelich, 2010], can alter cave drip
776 water temperature and consequently influence speleothem growth. In fact, Casteel and
777 Banner [2014] illustrate that seasonal temperature variations control calcite growth rates and
778 trace element ratios. We emphasise that significant and frequent in-cave evaporation and drip
779 water cooling is to be expected for near-entrance parts of caves that are located in present (or
780 past) low humidity environments. Figure 10 summarises the evaporative cooling potential at
781 Cathedral Cave. While there is a weak correlation between drip water cooling and RH the
782 data exhibits significant scattering which indicates that additional parameters affect the
783 cooling, e.g. flow path, drip rate and air circulation. We observed up to -1.8 °C at a RH of <
784 95 % for drip water that is exposed to the cave air. Unravelling the dependency of drip water
785 evaporative cooling on venting clearly requires further research.

786 While we illustrate that evaporative drip water cooling is caused by regular ingress of dry air
787 during summer (Figure 7A-C), in-cave evaporation also occurs during winter as the outside
788 air is permanently denser (Figure 7D-F). Our results prove that Cathedral Cave is well vented
789 near the entrance despite the lack of discernible air movement. Results also indicate that
790 moisture escapes from even the deepest parts of the cave (RH < 100 %, evaporation rate > 0
791 mm) but measurable influences on the drip water temperature were not detected.

792 It is well accepted that venting influences geochemical signatures [Spotl et al., 2005; Baldini
793 et al., 2008]. We point out that evaporation leads to isotopic enrichment of drip water
794 [Cuthbert et al., 2014b; Markowska et al., submitted], and that evaporative drip water cooling
795 could significantly influence chemical/isotopic signatures in speleothems [Kim and O'Neil,
796 1997]. This may be a further complication in reconciling clumped isotope thermometry Δ_{47}

797 based temperature proxies in speleothems with mean air temperature, as Δ_{47} will be affected
798 by the temperature of the water film from which the carbonate is precipitated [Affek et al.,
799 2008].

800 Our results are consistent with Perrier et al. [2010] in that ventilation related effects, such as
801 evaporation and associated cave rock and drip water temperature anomalies, are damped with
802 increasing distance from the entrance. However, the magnitude of venting will strongly
803 depend on the cave geomorphology [De Freitas et al., 1982]. In fact considerable air flow has
804 been reported within caves [Conn, 1966; McLean, 1971; Cigna and Forti, 1986], in particular
805 when multiple entries located at different vertical elevations are present [Faimon et al., 2012;
806 Gregoric et al., 2013]. Figure 10 presents the first quantification of the effects of evaporative
807 cooling of cave drip water. Our data is just from two drip sites in one cave, and further
808 empirical field data is needed to develop a predictive model of factors determining the extent
809 of evaporative cooling. However, the implications for speleothem temperature proxies are
810 clear – in ventilated caves, researchers should consider the possibility that the speleothem
811 proxy temperature is systematically cooler than the external mean air temperature.

812 **4.2.4. Considerations for the type of speleothem to be sampled**

813 A question arises as a result of the above discussion: What type of speleothem should be
814 sampled to best constrain the drip water temperature? Site 1 has a stalagmite fed from a
815 flowstone with a relatively long path (~3 m) where the water is exposed to the cave
816 atmosphere via film flow. While we expect this type of speleothem would have a large
817 potential for thermal disequilibrium affecting temperature proxies, it could still be a good
818 source for soil or vegetation derived signals (i.e., pollen). A stalagmite fed by a regular
819 conical-shaped stalactite will have drip water flowing along the outside of the deposit. This
820 type of speleothem would be cooled during periods when the drip rate is slow and regular
821 [Cuthbert et al., 2014a] which may imprint on the geochemical proxy and make interpretation
822 difficult. We believe that the best stalagmite (likely a candlestick shape) for sampling is fed
823 by a soda-straw stalactite because the flow path to the drip is surrounded by (thin) calcite and
824 the water is therefore less exposed to the cave atmosphere and potential evaporative cooling.
825 However, confirming this requires further research.

826 **4.2.5. Summary**

827 The implications of our results for speleothem paleoclimate reconstruction can be
828 summarised as follows:

- 829 ● The location that the proxy-derived temperature signal is representative for (i.e., surface
830 or drip source) and the processes that could influence the signal must be carefully
831 considered. Depending on the requirements, Equation 1 offers a quantitative model to
832 convolve or deconvolve the “background” temperature signal between surface and drip
833 source onto which in-cave signals will be superimposed.
- 834 ● The damping of surface temperature variations in the soil/epikarst is a function of
835 subsurface depth and frequency (Figure 9). If a surface temperature signal is required as a
836 paleoclimate proxy (i.e., a decadal-scale temperature signal) a near-surface chamber,
837 again with minimum venting and maximum relative humidity, should fulfil the conditions
838 for sampling.
- 839 ● Figure 9 illustrates the importance of considering the subsurface depth when speleothems
840 are sampled for the purpose of accurately unravelling the surface temperature signal from
841 isotope proxies. For example, highest amplitudes for the surface temperature during
842 glacial-interglacial climate transitions and for the variability over the last 10,000 years are
843 5 °C and 0.5-1 °C, respectively [Cheng et al., 2009]. A rough guide for selecting
844 appropriate sampling depths where the desired signal can be resolved is given in Table 5.
- 845 ● We stress that, consistent with the results of Cuthbert et al. [2014a], frequent evaporative
846 cooling events are to be expected in caves that could have been ventilated or exposed to
847 evaporation (RH < 100 %). Evaporative cooling can lower the drip water temperature
848 compared to cave air/speleothem temperature. The best cave locations to minimise this
849 effect are those with a long-term RH of 100 % and no air flow. These criteria were set out
850 in the 1960s to determine where to best sample speleothems for temperature records from
851 ¹⁸O [Hendy, 1971]. Here we show that, while the premise was correct, correction of the
852 temperature signal should be considered. The influence could be assessed by checking for
853 a difference in air and drip water temperature.
- 854 ● The best speleothems to sample and analyse to obtain paleoclimate records of surface air
855 temperature changes are minimum diameter stalagmites that are supplied by soda-straw
856 stalactites. While the speleothem-water contact is maximised over water-air contact, the
857 drip rates for these specimens are likely to be slow and evaporation could still occur, and
858 therefore caves of RH of 100% and no air flow would provide ideal sampling locations.

859 **5. Conclusion**

860 Cave drip water temperature is controlled by multiple heat transfer mechanisms acting
861 simultaneously during the movement of water through soil and bedrock and as film flow over
862 speleothem surfaces, i.e. conduction, convection and latent heat and mass exchange. The two
863 main heat sources/sinks are: 1) conduction of the dynamic surface temperature signal
864 vertically into the subsurface, 2) the cave atmosphere as is coupled to the surface atmosphere
865 by different venting mechanisms. The relative importance of each mechanism depends on the
866 thickness of the overburden, the distance of film flow between entering the cave and the
867 arriving at the drip source, and the advective velocity of the water film which is proportional
868 to the drip rate.

869 While cave air temperatures have been measured and analysed in detail, there is a general
870 lack of data and understanding relating to controls of cave drip water temperature. We
871 deployed multiple specialised high-resolution sensors along an in-cave flow path and drip
872 source to measure the evolution of the speleothem/water temperature. In-cave dripping was
873 induced through manual surface irrigation experiments with cooled water and deuterium as a
874 conservative tracer. In combination with measurements of drip rates, surface and cave
875 climate, in-cave evaporation rates and deuterium concentrations we identified and analysed,
876 for the first time, the heat transfer processes that exert control on the cave drip water
877 temperature between surface and drip source.

878 Temperature harmonics contained in the surface temperature signal propagate conductively
879 into the subsurface and undergo frequency dependent exponential amplitude damping and
880 linear phase shifting with subsurface depth. For example, we observed that there is a clear
881 exponential temperature-depth gradient induced by the annual surface temperature harmonic
882 which controls the drip water temperature (“background” temperature). Film flow along the
883 speleothem surface can convectively carry this signal down along the flow path causing
884 temperature anomalies that depend on the film advection rate (which is proportional to the
885 drip rate). However, this convective temperature anomaly is damped (“smeared”) by
886 conduction back into the speleothem along the flow path depending on the temperature-depth
887 gradient at the time.

888 At the same time the water film is exposed to the cave air which can significantly change drip
889 water temperature through convection/conduction or latent heat and mass exchange, with
890 magnitudes that depend on the distance from the cave entrance. The influence on the water

891 temperature, however, depends on the film advection rate and the complex coupling between
892 surface and cave climate through venting (i.e. air exchange induced by a density difference
893 between surface and cave air). We observed regular evaporative drip water cooling events of
894 $-1.5\text{ }^{\circ}\text{C}$ and up to $-2.5\text{ }^{\circ}\text{C}$ during summer when denser low-RH air enters the cave. Further,
895 the drip water temperature can also fluctuate due to air-induced convection/conduction in
896 winter when surface air is continuously denser (constant venting).

897 Drip water temperature is a key parameter controlling many biogeochemical in-cave
898 processes that must be quantified when the paleoclimate is reconstructed from speleothem-
899 based archives. We advise how the drip water “background” temperature can be modelled
900 using simple analytical solutions of the differential heat conduction equation. We show how a
901 data supported conceptual model for cave drip water temperature can assist with constraining
902 a range of temperature sensitive biogeochemical speleothem processes. Further, we offer
903 guidance on the type and location of speleothems that are sampled for paleoclimate signals
904 with the intent to either maximise or minimise the drip water temperature signature. We
905 anticipate that our findings will lead to significant improvements in the understanding of
906 climate signals from speleothem based paleoclimate archives.

907 **Acknowledgements**

908 Funding for this research was provided by the National Centre for Groundwater Research and
909 Training, an Australian Government initiative, supported by the Australian Research Council
910 and the National Water Commission. Funding was also provided by the Gary Johnston fund
911 that started the Chair of Water Management at UNSW. Mark Cuthbert was supported by
912 Marie Curie Research Fellowship funding from the European Community's Seventh
913 Framework Programme [FP7/2007-2013] under grant agreement n.299091. The climate
914 station, Stalagmates and the specialised temperature monitoring equipment were provided by
915 the Australian Government National Collaborative Research Infrastructure Strategy (NCRIS).
916 We thank: Evan Jensen, Chris George, Col Birchall, Mike Augee and Eliza Wells for
917 practical and logistical support during the irrigation experiments; Bruce Welsh and Philip
918 Maynard from Sydney University Speleological Society for the cave survey map; Mark
919 Whelan for help designing and building the high-resolution temperature equipment; Paul
920 Brockbank from the School of Chemical Engineering workshop for his precision in drilling
921 holes into a limestone sample so that thermal measurements could be conducted. The
922 manuscript was significantly improved thanks to feedback from Claude Hillaire-Marcel
923 (editor), Corrinne Wong (guest editor) and an anonymous reviewer.

924 **References**

- 925 Affek, H.P., Bar-Matthews, M., Ayalon, A., Matthews, A., Eiler, J.M., 2008.
926 Glacial/interglacial temperature variations in Soreq cave speleothems as recorded by
927 'clumped isotope' thermometry. *Geochimica et Cosmochimica Acta* 72, 5351-5360,
928 doi:<http://dx.doi.org/10.1016/j.gca.2008.06.031>.
- 929 Atkinson, T., Smart, P., Wigley, T., 1983. Climate and natural radon levels in Castleguard
930 cave, Columbia Icefields, Alberta, Canada. *Arctic and Alpine Research*, 487-502
- 931 Baker, A., Genty, D., Dreybrodt, W., Barnes, W.L., Mockler, N.J., Grapes, J., 1998. Testing
932 theoretically predicted stalagmite growth rate with recent annually laminated samples:
933 Implications for past stalagmite deposition. *Geochimica et Cosmochimica Acta* 62, 393-404
- 934 Baker, A.J., Matthey, D.P., Baldini, J.U.L., 2014. Reconstructing modern stalagmite growth
935 from cave monitoring, local meteorology, and experimental measurements of dripwater films.
936 *Earth and Planetary Science Letters* 392, 239-249,
937 doi:<http://dx.doi.org/10.1016/j.epsl.2014.02.036>.
- 938 Baker, D.G., Ruschy, D.L., 1993. The recent warming in eastern Minnesota shown by ground
939 temperatures. *Geophysical Research Letters* 20, 371-374
- 940 Baldini, J.U., McDermott, F., Hoffmann, D.L., Richards, D.A., Clipson, N., 2008. Very high-
941 frequency and seasonal cave atmosphere pCO₂ variability: Implications for stalagmite
942 growth and oxygen isotope-based paleoclimate records. *Earth and Planetary Science Letters*
943 272, 118-129
- 944 Bendjoudi, H., Cheviron, B., Guérin, R., Tabbagh, A., 2005. Determination of
945 upward/downward groundwater fluxes using transient variations of soil profile temperature:
946 test of the method with Voyons (Aube, France) experimental data. *Hydrological processes*
947 19, 3735-3745
- 948 BOM, 2014. Climate statistics for Australian locations: Wellington (Agrowplow). Bureau of
949 Meteorology, Australian Government.
950 http://www.bom.gov.au/climate/averages/tables/cw_065034_All.shtml, accessed: Dec 2014.
- 951 Buecher, R.H., 1999. Microclimate study of Kartchner caverns, Arizona. *Journal of Cave and*
952 *Karst Studies* 61, 108-120.
- 953 Carslaw, H.S., Jaeger, J.C., 1959. *Conduction of heat in solids*, 2nd ed. Clarendon Press,
954 Oxford. Camporeale, C., Ridolfi, L., 2012. Hydrodynamic-driven stability analysis of

955 morphological patterns on stalactites and implications for cave paleoflow reconstructions.
956 *Physical review letters* 108, 238501

957 Cheng, H., Edwards, R.L., Broecker, W.S., Denton, G.H., Kong, X., Wang, Y., Zhang, R.,
958 Wang, X., 2009. Ice Age Terminations. *Science* 326, 248-252, doi:10.1126/science.1177840.

959 Cheviron, B., Guérin, R., Tabbagh, A., Bendjoudi, H., 2005. Determining long-term effective
960 groundwater recharge by analyzing vertical soil temperature profiles at meteorological
961 stations. *Water resources research* 41

962 Clauser, C., Huenges, E., 1995. Thermal conductivity of rocks and minerals. *Rock Physics
963 and Phase Relations: A Handbook of Physical Constants* 3, 105-126,
964 doi:10.1029/RF003p0105.

965 Conn, H.W., 1966. Barometric wind in wind and jewel caves, South Dakota. *The national
966 speleological society bulletin* 28, 55-69

967 Covington, M.D., Luhmann, A.J., Gabrovšek, F., Saar, M.O., Wicks, C.M., 2011.
968 Mechanisms of heat exchange between water and rock in karst conduits. *Water Resources
969 Research* 47, W10514, doi:10.1029/2011WR010683.

970 Covington, M.D., Luhmann, A.J., Wicks, C.M., Saar, M.O., 2012. Process length scales and
971 longitudinal damping in karst conduits. *Journal of Geophysical Research: Earth Surface* 117,
972 F01025, doi:10.1029/2011JF002212.

973 Cuthbert, M.O., Baker, A., Jex, C.N., Graham, P.W., Treble, P.C., Andersen, M.S., Ian
974 Acworth, R., 2014b. Drip water isotopes in semi-arid karst: implications for speleothem
975 paleoclimatology. *Earth and Planetary Science Letters* 395, 194-204

976 Cuthbert, M.O., Rau, G.C., Andersen, M.S., Roshan, H., Rutledge, H., Marjo, C.E.,
977 Markowska, M., Jex, C.N., Graham, P.W., Mariethoz, G., Acworth, R.I., Baker, A., 2014a.
978 Evaporative cooling of speleothem drip water. *Scientific Reports* 4, doi:10.1038/srep05162.

979 Davis, B.A.S., Brewer, S., Stevenson, A.C., Guiot, J., 2003. The temperature of Europe
980 during the Holocene reconstructed from pollen data. *Quaternary Science Reviews* 22, 1701-
981 1716, doi:http://dx.doi.org/10.1016/S0277-3791(03)00173-2.

982 De Freitas, C., Littljohn, R., Clarkson, T., Kristament, I., 1982. Cave climate: assessment of
983 airflow and ventilation. *Journal of Climatology* 2, 383-397

984 De Freitas, C., Littlejohn, R., 1987. Cave climate: assessment of heat and moisture exchange.
985 *Journal of Climatology* 7, 553-569

986 De Freitas, C., Schmekal, A., 2003. Condensation as a microclimate process: measurement,
987 numerical simulation and prediction in the Glowworm Cave, New Zealand. *International*
988 *Journal of Climatology* 23, 557-575

989 De Vries, D.A., 1963. Thermal properties of soils. *Physics of plant environment*

990 Domínguez-Villar, D., Fairchild, I.J., Baker, A., Carrasco, R.M., Pedraza, J., 2013.
991 Reconstruction of cave air temperature based on surface atmosphere temperature and
992 vegetation changes: Implications for speleothem palaeoclimate records. *Earth and Planetary*
993 *Science Letters* 369, 158-168

994 Domínguez-Villar, D., Fairchild, I.J., Baker, A., Wang, X., Edwards, R.L., Cheng, H., 2009.
995 Oxygen isotope precipitation anomaly in the North Atlantic region during the 8.2 ka event.
996 *Geology* 37, 1095-1098, doi:10.1130/g30393a.1.

997 Domínguez-Villar, D., Lojen, S., Krklec, K., Baker, A., Fairchild, I.J., 2014. Is global
998 warming affecting cave temperatures? Experimental and model data from a paradigmatic
999 case study. *Climate Dynamics*, 1-13

1000 Dreybrodt, W., 1981. The kinetics of calcite precipitation from thin films of calcareous
1001 solutions and the growth of speleothems: revisited. *Chemical Geology* 32, 237-245

1002 Dreybrodt, W., Gabrovšek, F., Perne, M., 2005. Condensation corrosion: a theoretical
1003 approach. *Speleogenesis and Evolution of Karst Aquifers* 3

1004 Epstein, S., Buchsbaum, R., Lowenstam, H.A., Urey, H.C., 1953. Revised carbonate-water
1005 isotopic temperature scale. *Geological Society of America Bulletin* 64, 1315-1326

1006 Faimon, J., Troppová, D., Baldík, V., Novotný, R., 2012. Air circulation and its impact on
1007 microclimatic variables in the Císařská Cave (Moravian Karst, Czech Republic). *International*
1008 *Journal of Climatology* 32, 599-623

1009 Giacomo, P., 1982. Equation for the Determination of the Density of Moist Air (1981).
1010 *Metrologia* 18, 33

1011 Hendy, C.H., 1971. The isotopic geochemistry of speleothems—I. The calculation of the
1012 effects of different modes of formation on the isotopic composition of speleothems and their

1013 applicability as palaeoclimatic indicators. *Geochimica et Cosmochimica Acta* 35, 801-824,
1014 doi:[http://dx.doi.org/10.1016/0016-7037\(71\)90127-X](http://dx.doi.org/10.1016/0016-7037(71)90127-X).

1015 Holmes, J., Lowe, J., Wolff, E., Srokosz, M., 2011. Rapid climate change: lessons from the
1016 recent geological past. *Global and Planetary Change* 79, 157-162,
1017 doi:10.1016/j.gloplacha.2010.10.005.Horai, K.-i., 1971. Thermal Conductivity of Rock-
1018 Forming Minerals. *Journal of Geophysical Research* 76, 1278-1308,
1019 doi:10.1029/JB076i005p01278.

1020 Jex, C.N., Mariethoz, G., Baker, A., Graham, P., Andersen, M.S., Acworth, I., Edwards, N.,
1021 Azcurra, C., 2012. Spatially dense drip hydrological monitoring and infiltration behaviour at
1022 the Wellington Caves, South East Australia. *International Journal of Speleology* 41, 14

1023 Kim, S.-T., O'Neil, J.R., 1997. Equilibrium and nonequilibrium oxygen isotope effects in
1024 synthetic carbonates. *Geochimica et Cosmochimica Acta* 61, 3461-3475,
1025 doi:[http://dx.doi.org/10.1016/S0016-7037\(97\)00169-5](http://dx.doi.org/10.1016/S0016-7037(97)00169-5).

1026 Kowalczyk, A.J., Froelich, P.N., 2010. Cave air ventilation and CO₂ outgassing
1027 by radon-222 modeling: How fast do caves breathe? *Earth and Planetary Science Letters* 289,
1028 209-219.

1029 Luhmann, A.J., Covington, M.D., Myre, J.M., Perne, M., Jones, S.W., Alexander Jr, E.C.,
1030 Saar, M.O., 2015. Thermal damping and retardation in karst conduits. *Hydrol. Earth Syst.*
1031 *Sci.* 19, 137-157, doi:10.5194/hess-19-137-2015.

1032 Mariethoz, G., Baker, A., Sivakumar, B., Hartland, A., Graham, P., 2012. Chaos and
1033 irregularity in karst percolation. *Geophysical Research Letters* 39

1034 Markowska, M., Baker, A., Andersen, M.S., Jex, C.N., Graham, P.W., Cuthbert, M.O., Rau,
1035 G.C., Rutledge, H., Mariethoz, G., Marjo, C.E., Treble, P.C., Edwards, N., submitted. It's all
1036 about evaporation: artificial and natural water isotope tracing in semi-arid karst. *Quaternary*
1037 *Science Reviews*

1038 McLean, J.S., 1971. The microclimate in Carlsbad Caverns, New Mexico. US Geological
1039 Survey, Albuquerque, New Mexico.

1040 NIST, 2014. NIST Chemistry WebBook. National Institute of Standards and Technology,
1041 U.S. Department of Commerce. <http://webbook.nist.gov/>, accessed: Dec 2014.

1042 Northup, E., Lavoie, K.H.D., 2001. Geomicrobiology of caves: a review. *Geomicrobiology*
1043 *Journal* 18, 199-222

1044 Ochsner, T.E., Horton, R., Ren, T., 2001. A New Perspective on Soil Thermal Properties.
1045 Soil Sci. Soc. Am. J. 65, 1641-1647, doi:10.2136/sssaj2001.1641.

1046 Oh, Y.H., Kim, G., 2011. Factors controlling the air ventilation of a limestone cave revealed
1047 by ^{222}Rn and ^{220}Rn tracers. *Geosciences Journal* 15, 115-119

1048 Orland, I.J., Bar-Matthews, M., Kita, N.T., Ayalon, A., Matthews, A., Valley, J.W., 2009.
1049 Climate deterioration in the Eastern Mediterranean as revealed by ion microprobe analysis of
1050 a speleothem that grew from 2.2 to 0.9 ka in Soreq Cave, Israel. *Quaternary Research* 71, 27-
1051 35, doi:http://dx.doi.org/10.1016/j.yqres.2008.08.005.

1052 Osborne, R., 2007. Cathedral Cave, Wellington Caves, New South Wales, Australia. A
1053 multiphase, non-fluvial cave. *Earth Surface Processes and Landforms* 32, 2075-2103

1054 Perrier, F., Le Mouél, J.-L., Richon, P., 2010. Spatial and Temporal Dependence of
1055 Temperature Variations Induced by Atmospheric Pressure Variations in Shallow
1056 Underground Cavities. *Pure and applied geophysics* 167, 253-276

1057 Rau, G.C., Andersen, M.S., McCallum, A.M., Roshan, H., Acworth, R.I., 2014. Heat as a
1058 tracer to quantify water flow in near-surface sediments. *Earth-Science Reviews* 129, 40-58

1059 Rutledge, H., Baker, A., Marjo, C.E., Andersen, M.S., Graham, P.W., Cuthbert, M.O., Rau,
1060 G.C., Roshan, H., Markowska, M., Mariethoz, G., Jex, C.N., 2014. Dripwater organic matter
1061 and trace element geochemistry in a semi-arid karst environment: Implications for
1062 speleothem paleoclimatology. *Geochimica et Cosmochimica Acta* 135, 217-230,
1063 doi:10.1016/j.gca.2014.03.036.

1064 Schärli, U., Rybach, L., 2001. Determination of specific heat capacity on rock fragments.
1065 *Geothermics* 30, 93-110, doi:10.1016/S0375-6505(00)00035-3.

1066 Schön, J.H., 1996. *Physical Properties of Rocks: Fundamentals and Principles of*
1067 *Petrophysics*. 583

1068 Schouten, S., Woltering, M., Rijpstra, W.I.C., Sluijs, A., Brinkhuis, H., Sinninghe Damsté,
1069 J.S., 2007. The Paleocene–Eocene carbon isotope excursion in higher plant organic matter:
1070 Differential fractionation of angiosperms and conifers in the Arctic. *Earth and Planetary*
1071 *Science Letters* 258, 581-592

1072 Smerdon, J.E., Pollack, H.N., Cermak, V., Enz, J.W., Kresl, M., Safanda, J., Wehmiller, J.F.,
1073 2004. Air-ground temperature coupling and subsurface propagation of annual temperature
1074 signals. *Journal of Geophysical Research: Atmospheres* (1984–2012) 109

1075 Smerdon, J.E., Pollack, H.N., Enz, J.W., Lewis, M.J., 2003. Conduction-dominated heat
1076 transport of the annual temperature signal in soil. *Journal of Geophysical Research: Solid*
1077 *Earth* (1978–2012) 108

1078 Smithson, P., 1991. Inter-relationships between cave and outside air temperatures.
1079 *Theoretical and applied climatology* 44, 65-73

1080 Spötl, C., Fairchild, I.J., Tooth, A.F., 2005. Cave air control on dripwater geochemistry, Obir
1081 Caves (Austria): Implications for speleothem deposition in dynamically ventilated caves.
1082 *Geochimica et Cosmochimica Acta* 69, 2451-2468

1083 Tabbagh, A., Bendjoudi, H., Benderitter, Y., 1999. Determination of recharge in unsaturated
1084 soils using temperature monitoring. *Water resources research* 35, 2439-2446

1085 Tarhule-Lips, R.F., Ford, D.C., 1998. Condensation corrosion in caves on Cayman Brac and
1086 Isla de Mona. *Journal of caves and karst studies* 60, 84-95

1087 Tarnawski, V.R., Momose, T., Leong, W.H., 2011. Thermal Conductivity of Standard Sands
1088 II. Saturated Conditions. *International Journal of Thermophysics* 32, 984-1005,
1089 doi:10.1007/s10765-011-0975-1.

1090 Treble, P.C., Schmitt, A.K., Edwards, R.L., McKeegan, K.D., Harrison, T.M., Grove, M.,
1091 Cheng, H., Wang, Y.J., 2007. High resolution Secondary Ionisation Mass Spectrometry
1092 (SIMS) $\delta^{18}\text{O}$ analyses of Hulu Cave speleothem at the time of Heinrich Event 1. *Chemical*
1093 *Geology* 238, 197-212, doi:http://dx.doi.org/10.1016/j.chemgeo.2006.11.009.

1094 Vosteen, H.-D., Schellschmidt, R., 2003. Influence of temperature on thermal conductivity,
1095 thermal capacity and thermal diffusivity for different types of rock. *Physics and Chemistry of*
1096 *the Earth, Parts A/B/C* 28, 499-509, doi:http://dx.doi.org/10.1016/S1474-7065(03)00069-X.

1097 Wigley, T., 1967. Non-steady flow through a porous medium and cave breathing. *Journal of*
1098 *Geophysical Research* 72, 3199-3205

1099 Yan, W.-M., Soong, C.-Y., 1995. Convective heat and mass transfer along an inclined heated
1100 plate with film evaporation. *International Journal of Heat and Mass Transfer* 38, 1261-1269,
1101 doi:http://dx.doi.org/10.1016/0017-9310(94)00241-M.

1102

1103 **Figure captions:**

1104 Figure 1: Survey map of Cathedral Cave located in the Wellington Caves Reserve in NSW,
1105 Australia. Instrumented sites are marked with red on the map.

1106

1107 Figure 2: A) Schematic subsurface cross-section of Site A (Figure 1) showing the drip water
1108 flow path along a flow stone to the stalactite (drip site) and the sensors deployed to measure
1109 water film and drip temperature and cave air temperature as well as climate parameters
1110 (humidity and pressure). B) A StarOddi micro T temperature sensor measuring at the drip
1111 source. C) Example of high-precision aluminium temperature sensor mounted on flow stone
1112 along the flow path (Australian 1-dollar coin with 25 mm diameter for scale).

1113

1114 Figure 3: Data from two years of monitoring at the Cathedral Cave: Surface air temperature,
1115 daily precipitation, and cave air temperature (measured at Site A1 Figure 1). For air
1116 temperatures, best fit to Equation 1 is indicated by dashed black lines. Blue lines are the drip
1117 water temperatures measured at Site A. Vertical dark grey bars show the times at which
1118 surface irrigation experiments were conducted coinciding with intense data collection
1119 periods. The light grey background indicates the times at which longer-term cave flowstone
1120 and drip water temperature was measured. The blue lines are speleothem and drip water
1121 temperature measurements enlarged in Figure 6 and explained later.

1122

1123 Figure 4: Drip monitoring with high time-resolution at site A during summer 2014. A)
1124 Temperature measured along a drip water flow path (for locations see Fig. 2a) on top of the
1125 flowstone (blue), at ~40 mm depth into the flowstone (red) and in the air (green). Surface air
1126 temperature is also plotted (grey). B) Drip rate and relative humidity. A total of 2 irrigations
1127 were conducted (vertical black lines indicating equivalent rainfall) with 3400 L and 2400 L
1128 applied to the surface irrigation patch. Parts of this data were previously published in
1129 Cuthbert et al. [2014a] to demonstrate evaporative cooling of speleothems. Light grey shaded
1130 areas indicate periods dominated by evaporative cooling. Dark grey shaded areas depict
1131 periods dominated by film convection.

1132

1133 Figure 5: Drip monitoring with high time-resolution at site A during summer 2013. A total of
1134 4 irrigations were conducted with rainfall equivalents of 35 mm and 63 mm. A) Temperature
1135 measured at the tip of two neighbouring stalactites, and in the air (see Figure 2 for locations).
1136 Irrigations 1, 2 and 3 were cooled using bags with ice (irrigation water temperature is
1137 indicated next to the vertical black lines in a). B) Vertically enlarged temperature data from
1138 A. C) Deuterium measured in drip water samples during the irrigation experiment. Deuterium
1139 was added to the first irrigation (~6100 ‰ VSMOW). Min/max of the 2-year average from
1140 various drip sources at site A [Markowska et al., submitted]. D) Drip rate of both stalactites.
1141 The grey arrow (A and B) depicts the time when the surface air temperature was lower than
1142 the cave air temperature indicating cave venting. The blue arrow (B) shows the time at which
1143 the cooled surface irrigation caused a drip water temperature anomaly. Light grey shaded
1144 areas indicate periods of evaporative cooling. Dark grey shaded areas depict periods of film
1145 convection.

1146

1147 Figure 6: Temperatures measured at Site A on the flowstone surface where film flow
1148 occurred during times at which the drip source is active. Locations of the records are marked
1149 according to Figure 2. Data framed by grey vertical bars are highlighted in Figure 7. The
1150 highlighted winter dataset coincides with the surface irrigation experiment 3 (see also Figure
1151 3).

1152

1153 Figure 7: Summer (A-C) and winter (D-F) snapshots of dry/wet speleothem and cave air
1154 temperature (A and D), cave climate (B and E), surface and cave air density (C and F). Note
1155 that the winter dataset (D-F) shows the response to surface irrigation experiment 3 (see
1156 Figure 3). Note that y-axes of subplot B, C, E and F have the same range for better signal
1157 comparison.

1158

1159 Figure 8: Conceptual model of the different controls on cave drip water temperature between
1160 surface and drip source. Individual heat and mass transfer mechanisms are depicted by arrows
1161 and described as follows: $q_{c,am}$ is conduction between surface and subsurface, $q_{f,surf}$ is
1162 convection between surface and subsurface, $q_{f,am}$ is convection between surface and cave
1163 air, m_{am} is moisture exchange between surface and cave air, $q_{c,rock}$ is conduction between
1164 speleothem and water film, $q_{c,air}$ is conduction between water film and air, $q_{l,air}$ is latent heat

1165 exchange between water film and air, m_{air} is moisture exchange between water film and air,
1166 q_f is convection of the water film, v_f is advection of the water film, L is the film flow
1167 distance between water entering the cave and drip source, b is the thickness of the water
1168 film.

1169

1170 Figure 9: Depth penetration of surface temperature components based on Equations 1-2 and
1171 thermal parameters in Table 2 with selected frequencies (daily, annual, decadal, centennial
1172 and millennial): A) amplitude damping, B) phase shift. The grey bands enveloping the curves
1173 reflect the variability arising from min/max thermal parameters reported in the literature. The
1174 red dots illustrate practical examples given in the discussion.

1175

1176 Figure 10: The evaporative cooling potential: Difference between cave air and drip water
1177 temperature plotted against RH. Site A: ~2 months of summer data (Figure 6). Site B: Data
1178 from the irrigation experiment 2 (Figure 3B in Cuthbert et al. [2014a]). Site C: ~4 months of
1179 measurements.

1180 **Table captions:**

1181 Table 1: Detailed summary of the individual surface irrigations conducted at 3 different times
1182 over a two year period between 2013 and 2014.

1183

1184 Table 2: Summary of thermal parameters of water, air, soil and limestone: ¹Water and air
1185 properties can be found in NIST [2014]. ²Soil and limestone properties were measured in the
1186 laboratory using samples collected in the field. ³Ranges for soil thermal parameters and
1187 limestone bedrock are from Ochsner et al. [2001] and Vosteen and Schellschmidt [2003].

1188

1189 Table 3: Cave evaporation rates measured at different locations and opposing seasons.

1190

1191 Table 4: Summary of results obtained by analysing temperature data from different locations
1192 with Equation 1 using an annual signal period ($P = 365.25$ days), soil zone thickness $d = 0.1$
1193 m (except for surface air temperature), soil and limestone thermal diffusivity listed in Table
1194 2. Phase offset is relative to summer solstice. The fitting algorithm minimised the NRMSE by
1195 varying the bold parameters.

1196

1197 Table 5: Max/min damping factors (ratio between subsurface and surface amplitude) and
1198 signal shifts for distinct depths and different harmonic signals extracted from Figure 9.

Date	Experiment / application	Water volume [litres]	Equiv. rain [mm]	Duration of irrigation [hours]	Equiv. rainfall intensity [mm/h]	Irrigation water temperature [°C]
8/01/2013	1/1	840	~35	1.75	~20	0.3
9/01/2013	1/2	1500	~63	1.75	~35	10.6
10/01/2013	1/3	840	~35	1.75	~20	0.3
11/01/2013	1/4	1500	~63	1.75	~35	24.2
14/01/2014	2/1	3400	~68	2.85	~24	~25
15/01/2014	2/2	2400	~48	3.00	~16	~25
22/07/2014	3/1	1460	~29	1.00	~29	~12
23/07/2014	3/2	745	~15	0.50	~30	~12
24/07/2014	3/3	1460	~29	1.00	~29	~12

Table 1: Detailed summary of the individual surface irrigations conducted at 3 different times over a two year period between 2013 and 2014.

Material	Thermal conductivity [W/m/K]	Specific heat capacity [MJ/m ³ /K]	Thermal diffusivity [m ² /d]	Min. thermal diffusivity [m ² /d]	Max. thermal diffusivity [m ² /d]
Water @ 18 °C	0.595 ¹	4.180 ¹	0.0123 ¹	-	-
Air @ 18 °C	0.025 ¹	0.001 ¹	1.8014 ¹	-	-
Soil (dry)	0.545 ²	1.188 ²	0.0396 ²	-	-
Soil (saturated)	0.835 ²	2.939 ²	0.0245 ²	-	-
Soil	-	-	0.03 ³	0.01 ³	0.06 ³
Limestone	2.356 ²	2.518 ²	0.0808 ²	0.06 ³	0.14 ³

Table 2: Summary of thermal parameters of water, air, soil and limestone: ¹Water and air properties can be found in NIST [2014]. ²Soil and limestone properties were measured in the laboratory using samples collected in the field. ³Ranges for soil thermal parameters and limestone bedrock are from Ochsner et al. [2001] and Vosteen and Schellschmidt [2003].

Evaporation rate [mm/year]		
Location	Summer (January 2014)	Winter (July 2014)
Near entrance	440	
Site A	50	>56
Site B	40	
Site C	13	4.8

Table 3: Cave evaporation rates measured at different locations and opposing seasons.

Temperature measurement location	Mean	Amplitude	Phase	Phase offset	Total depth	NRMSE	Number of data points
Parameter [unit]	T_0 [°C]	A [°C]	[d]	θ [d]	z [m]	[-]	[-]
Surface air	16.90	8.51	0	20.0	0	0.1827	52,376
Flowstone (b, Site A)	17.18	5.03	30.7	31.9	1.55	0.2579	30,810
Flowstone (c, Site A)	16.62	4.11	42.4	31.8	2.16	0.2341	30,811
Stalactite (j, Site A)	16.11	2.61	68.8	31.2	3.55	0.1653	30,814
Cave air (Site A)	16.32	2.38	74.1	31.4	3.83	0.3609	23,750
Cave air (Site A1)	15.70	1.65	95.6	31.1	4.95	0.3400	29,338
Cave air (Site C)	18.10	-	-	-	~25	-	17,959

Table 4: Summary of results obtained by analysing temperature data from different locations with Equation 1 using an annual signal period ($P = 365.25$ days), soil zone thickness $d = 0.1$ m (except for surface air temperature), soil and limestone thermal diffusivity listed in Table 2. Phase offset is relative to summer solstice. The fitting algorithm minimised the NRMSE by varying the bold parameters.

Harmonic		daily		annual		decadal		centennial		millennial	
Depth [m]		Min	Max	Min	Max	Min	Max	Min	Max	Min	Max
0.1	Amp [-]	0.17	0.49	0.91	0.96	0.97	0.99	0.99	1.00	1.00	1.00
	Phase [months]	0.0	0.0	0.1	0.1	0.3	0.4	0.9	1.3	2.8	4.0
1	Amp [-]	0	0.01	0.65	0.77	0.87	0.92	0.96	0.97	0.99	1.00
	Phase [months]	-	0	0.5	0.8	1.6	2.5	5.1	7.8	16.3	24.5
10	Amp [-]	0	0	0.02	0.08	0.30	0.46	0.68	0.78	0.89	0.92
	Phase [months]	-	-	4.8	7.3	15.1	23.0	47.8	72.8	151.0	230.3
100	Amp [-]	0	0	0	0	0	0	0.02	0.08	0.30	0.46
	Phase [months]	-	-	-	-	-	-	473	723	1498	2288

Table 5: Max/min damping factors (ratio between subsurface and surface amplitude) and signal shifts for distinct depths and different harmonic signals extracted from Figure 9.

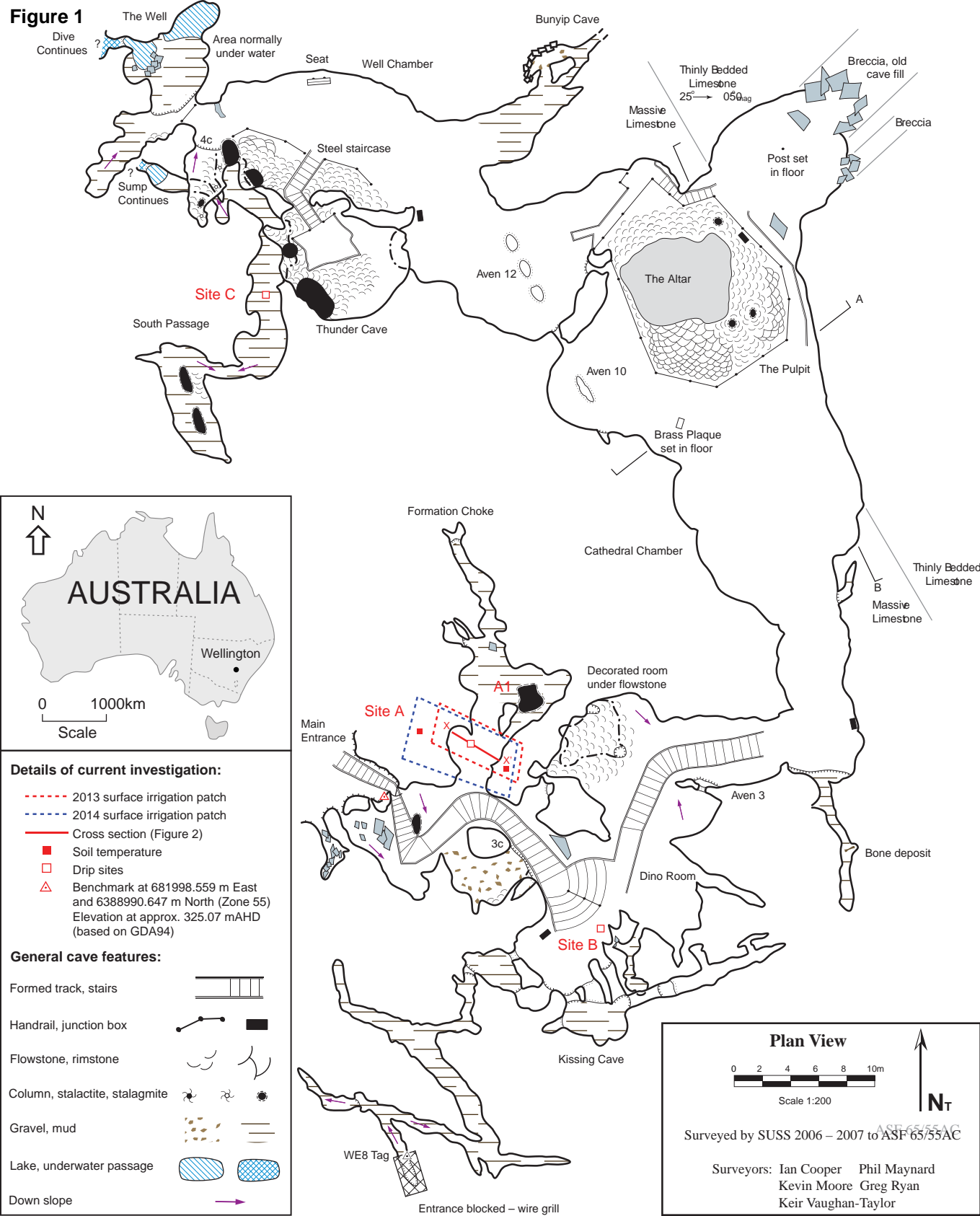
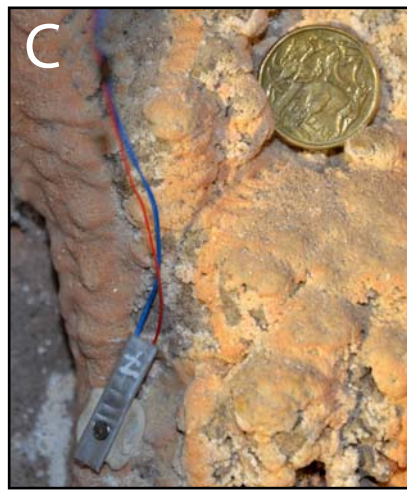
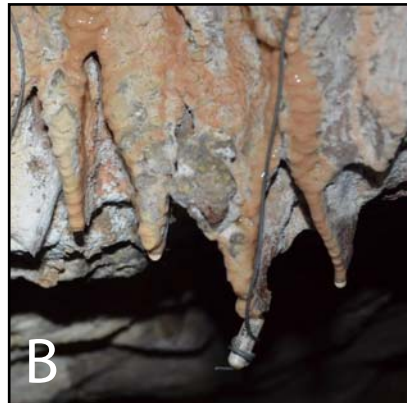
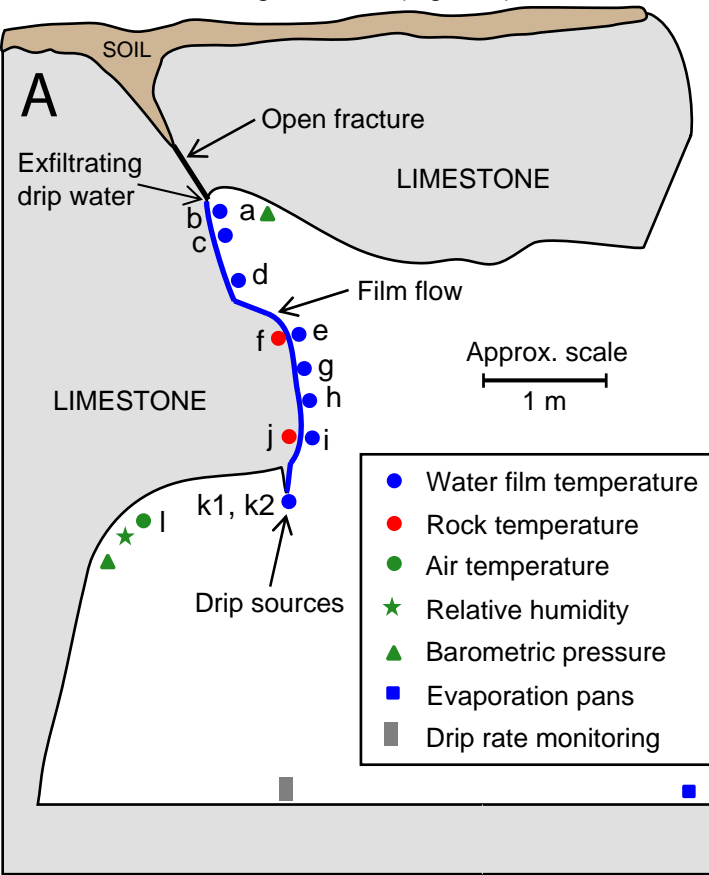
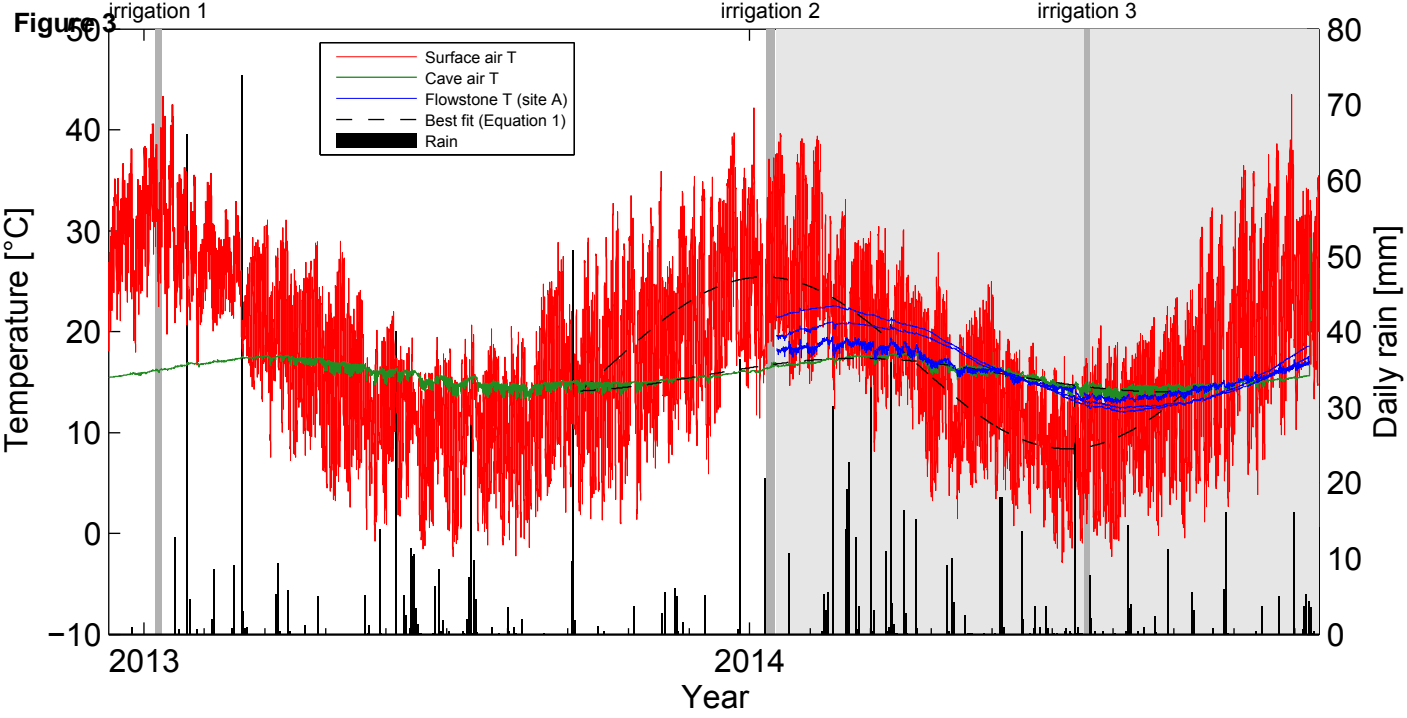
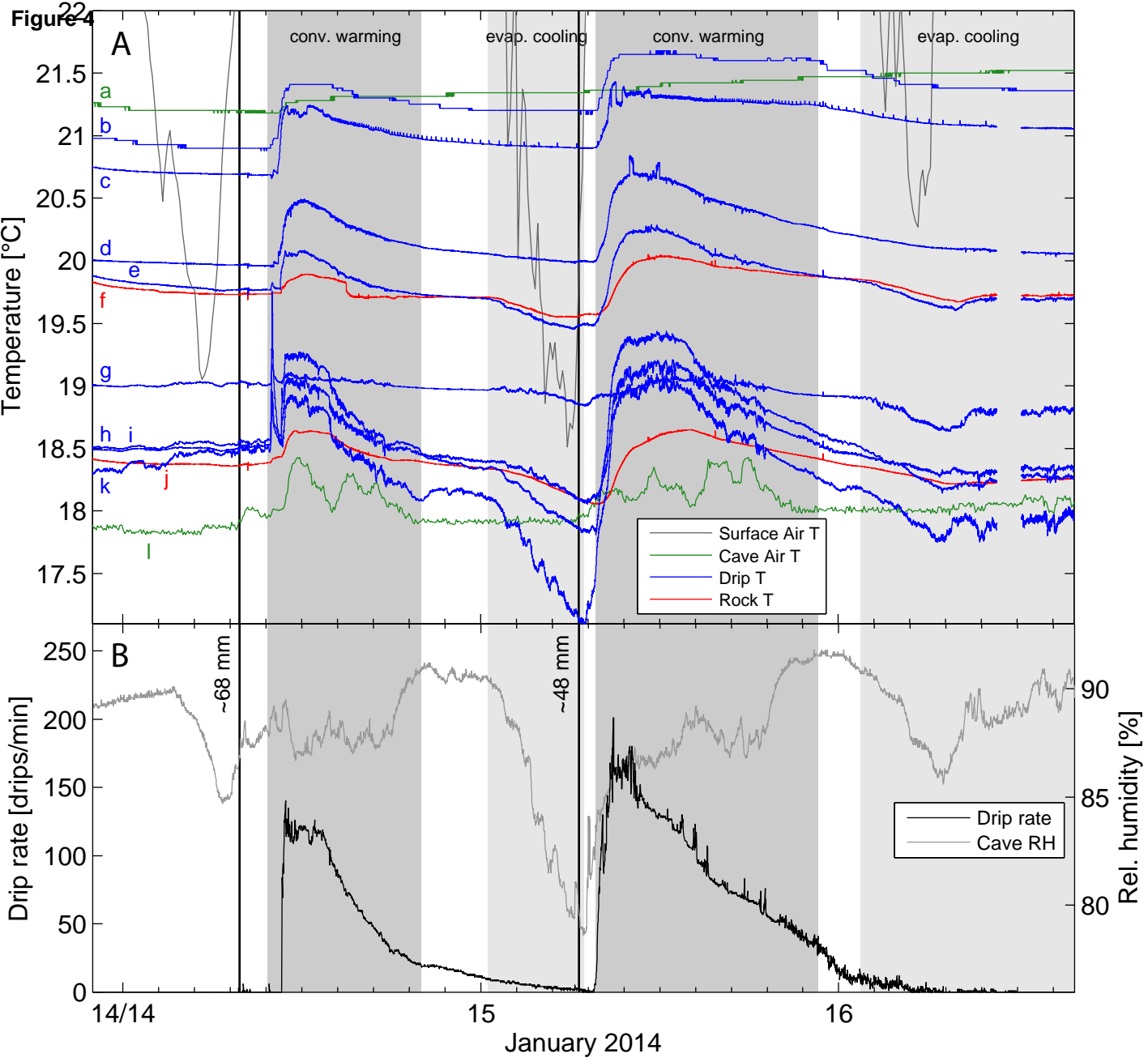
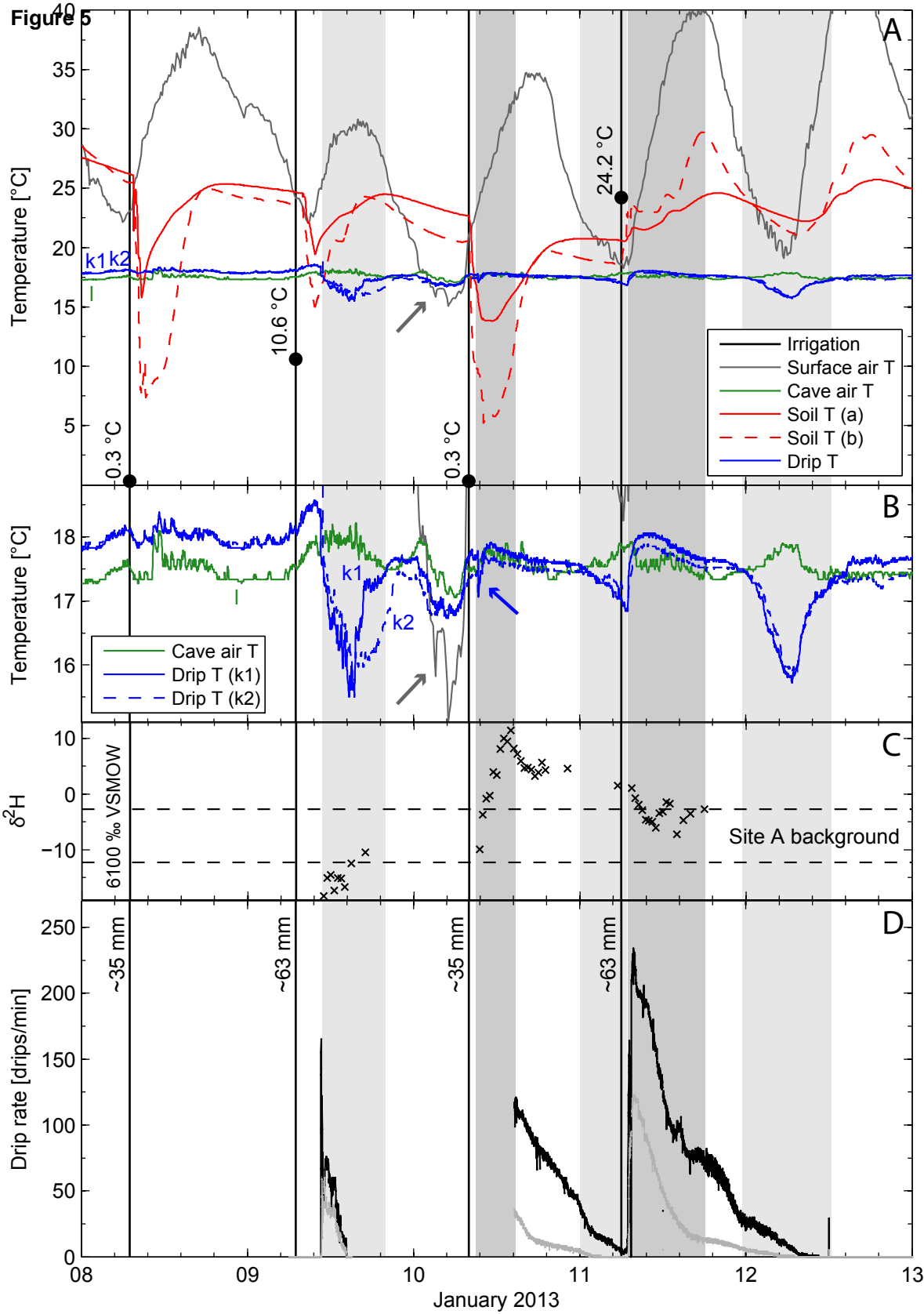


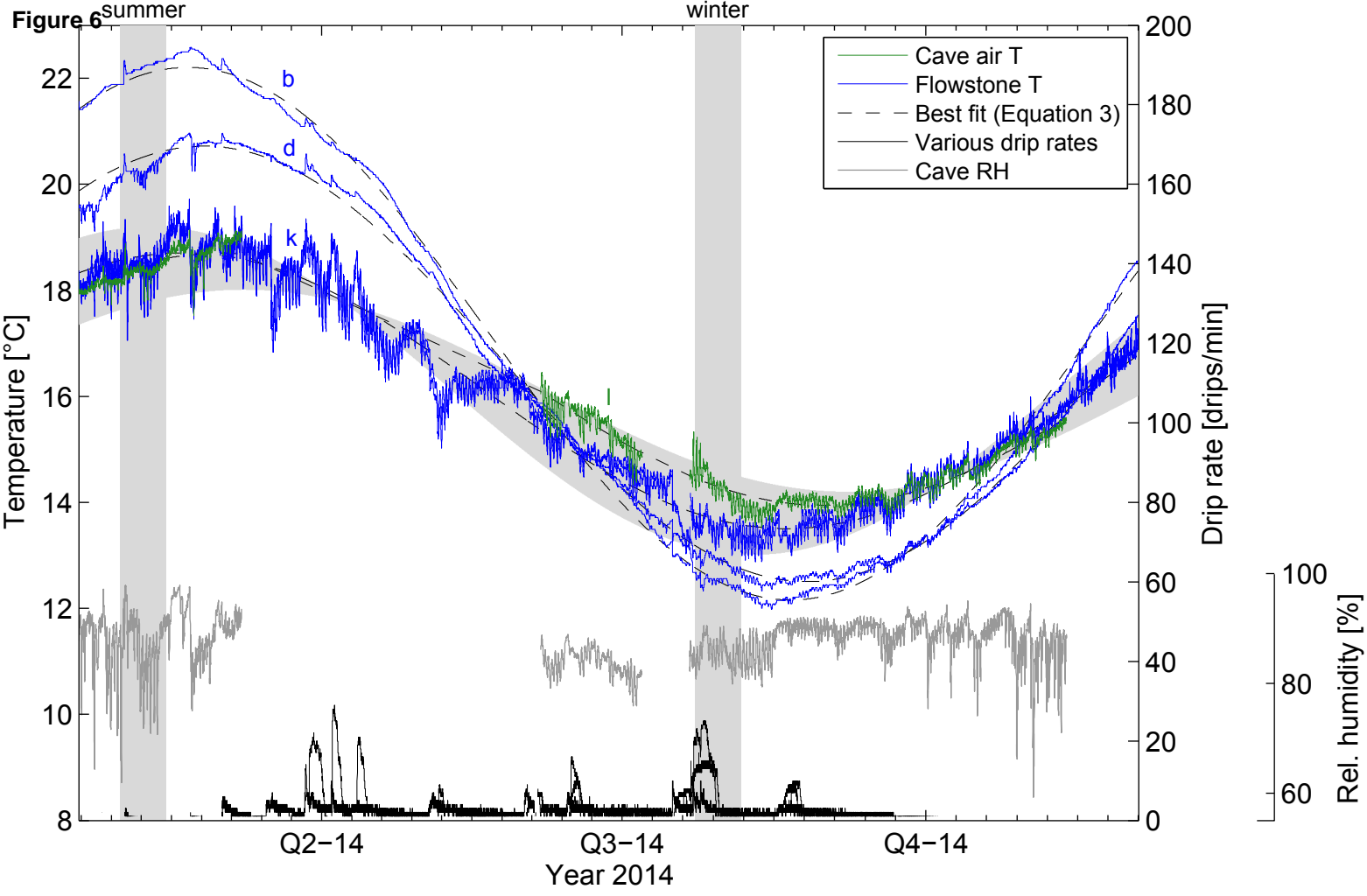
Figure 2 Surface irrigation area (Figure 1) **X'**











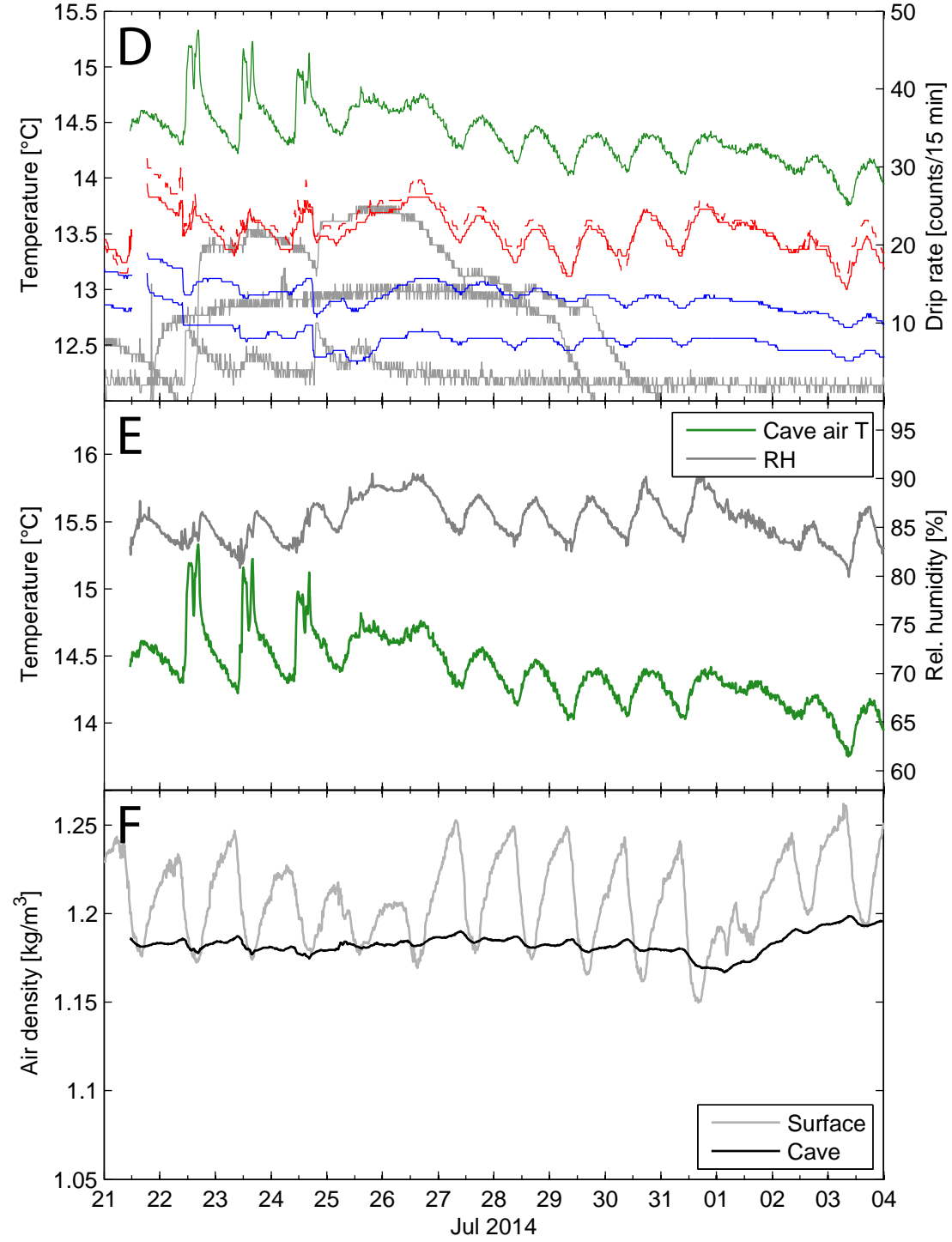
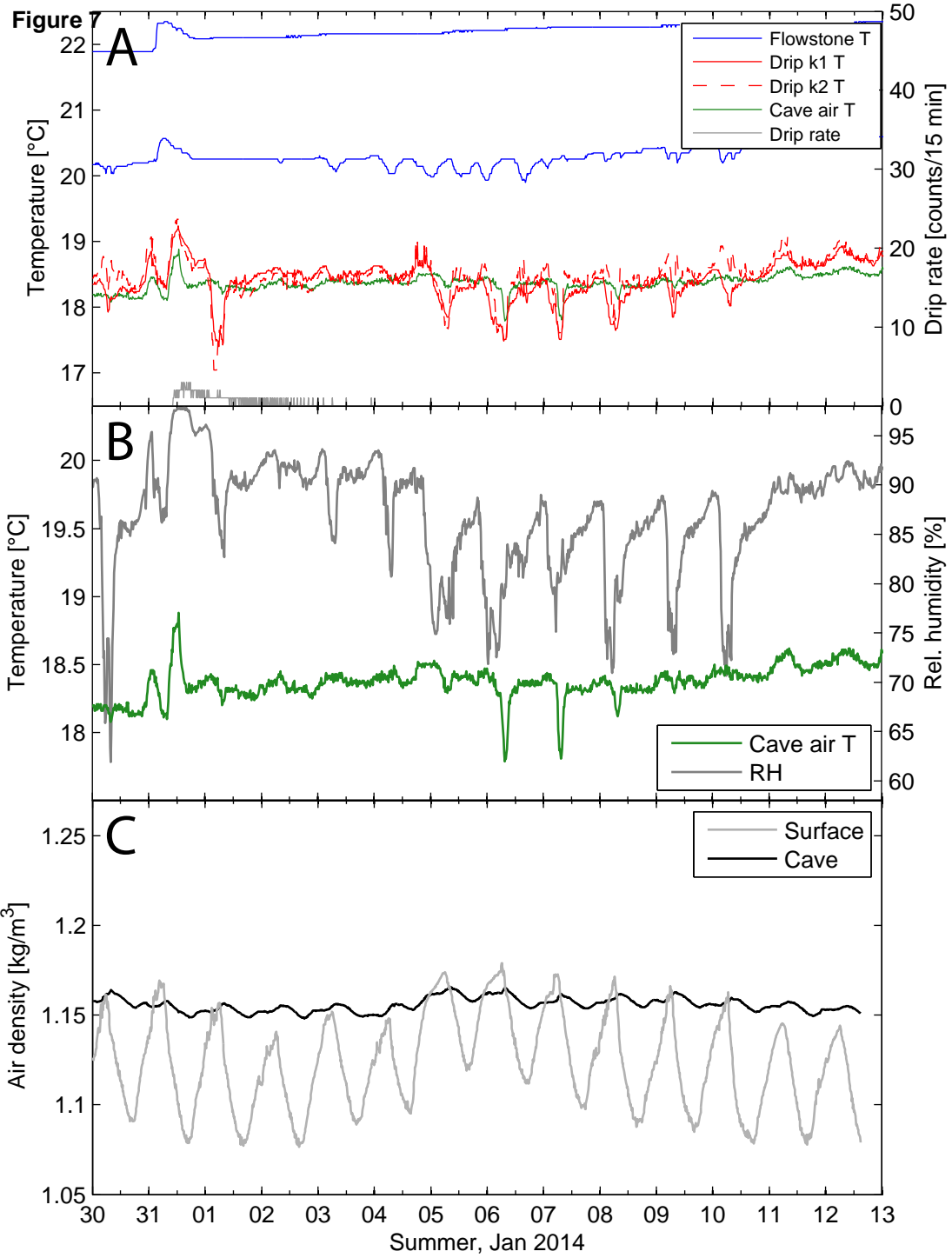
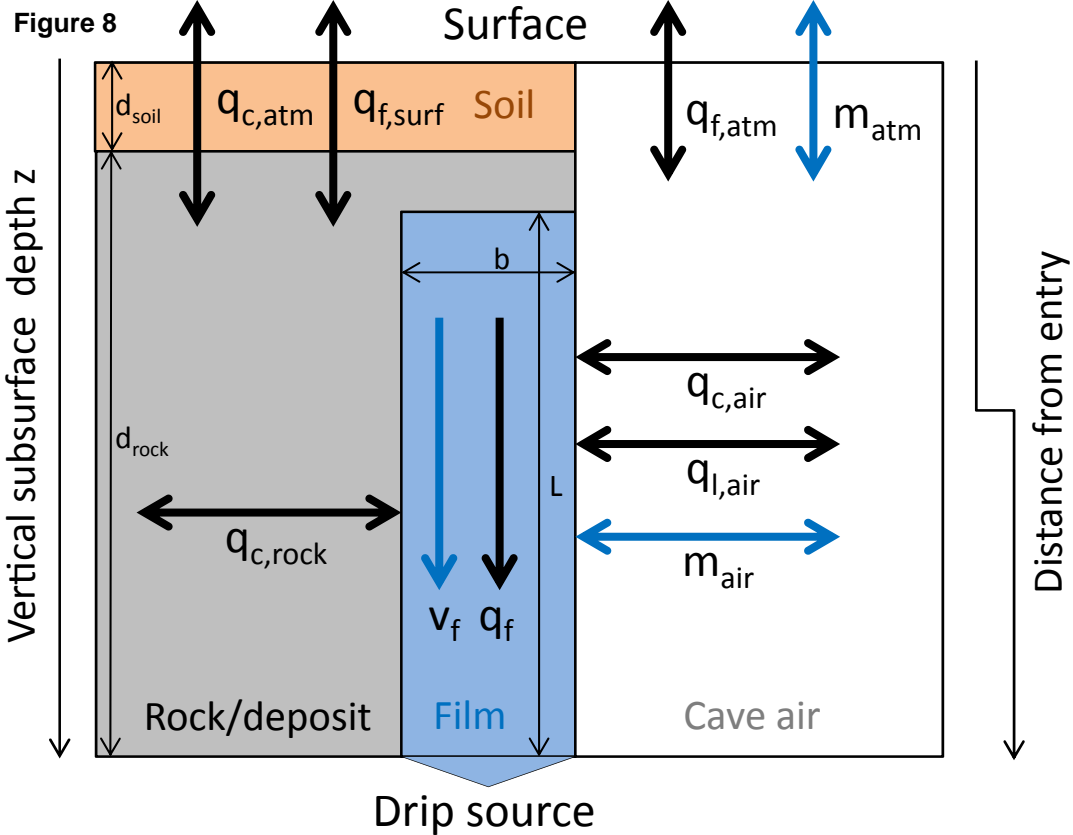


Figure 8

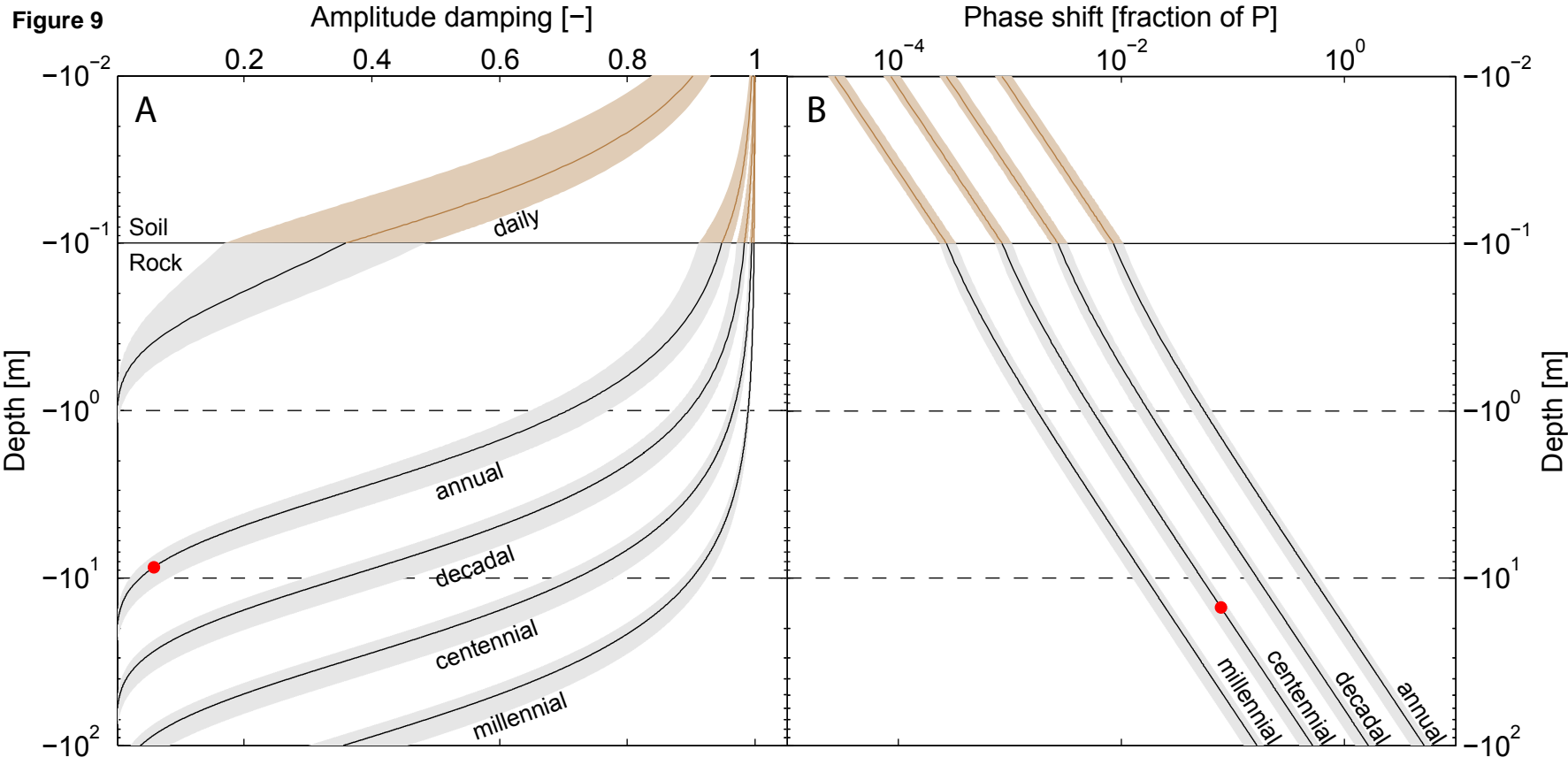


Figure 10

